

Connecting the X-ray properties of weak-line and typical quasars: testing for a geometrically thick accretion disk

Q. Ni,^{1*} W. N. Brandt,^{1,2,3} B. Luo,^{4,5} P. B. Hall,⁶ Yue Shen,⁷ S. F. Anderson,⁸
R. M. Plotkin,⁹ Gordon T. Richards,¹⁰ D. P. Schneider,^{1,2} O. Shemmer¹¹ and J. Wu¹²

¹Department of Astronomy & Astrophysics, Davey Lab, The Pennsylvania State University, University Park, PA 16802, USA

²Institute for Gravitation and the Cosmos, The Pennsylvania State University, University Park, PA 16802, USA

³Department of Physics, 104 Davey Lab, The Pennsylvania State University, University Park, PA 16802, USA

⁴School of Astronomy and Space Science, Nanjing University, Nanjing, Jiangsu 210093, China

⁵Key Laboratory of Modern Astronomy and Astrophysics (Nanjing University), Ministry of Education, Nanjing, Jiangsu 210093, China

⁶Department of Physics & Astronomy, York University, 4700 Keele Street, Toronto, ON M3J 1P3, Canada

⁷Department of Astronomy, University of Illinois at Urbana-Champaign, Urbana, IL 61801, USA

⁸Department of Astronomy, University of Washington, Box 351580, Seattle, WA 98195, USA

⁹International Centre for Radio Astronomy Research – Curtin University, GPO Box U1987, Perth, WA 6845, Australia

¹⁰Department of Physics, Drexel University, 32 S. 32nd Street, Philadelphia, PA 19104, USA

¹¹Department of Physics, University of North Texas, Denton, TX 76203, USA

¹²Department of Astronomy, Xiamen University, Xiamen, Fujian 361005, China

Accepted XXX. Received YYY; in original form ZZZ

ABSTRACT

We present X-ray and multiwavelength analyses of 32 weak emission-line quasars (WLQs) selected in a consistent and unbiased manner. New *Chandra* 3.1–4.8 ks observations were obtained for 14 of these WLQs with C IV rest-frame equivalent widths (REWs) of 5–15 Å, and these serve as an X-ray observational “bridge” between previously studied WLQs with C IV REW $\lesssim 5$ Å and more-typical quasars with C IV REW ≈ 15 –100 Å. We have identified and quantified a strong dependence of the fraction of X-ray weak quasars upon C IV REW; this fraction declines by a factor of ≈ 13 (from $\approx 44\%$ to $\approx 3\%$) for C IV REW ranging from 4–50 Å, and the rate of decline appears particularly strong in the 10–20 Å range. The dependence broadly supports the proposed “shielding” model for WLQs, in which a geometrically and optically thick inner accretion disk, expected for a quasar accreting at a high Eddington ratio, both prevents ionizing EUV/X-ray photons from reaching the high-ionization broad emission-line region and also sometimes blocks the line-of-sight to the central X-ray emitting region. This model is also supported by the hard average spectral shape of X-ray weak WLQs (with a power-law effective photon index of $\Gamma_{\text{eff}} = 1.19_{-0.45}^{+0.56}$). Additionally, we have examined UV continuum/emission-line properties that might trace X-ray weakness among WLQs, confirming that red UV continuum color is the most-effective tracer.

Key words: galaxies: active – galaxies: nuclei – quasars: general – X-rays: galaxies

1 INTRODUCTION

1.1 The importance, X-ray properties, and current interpretation of weak-line quasars

Strong and broad line emission is a defining characteristic of quasar spectra in the optical and ultraviolet (UV). However, the Sloan Digital Sky Survey (SDSS) (York et al. 2000) has discovered a remarkable population of ≈ 200 type 1 quasars

with strikingly weak or no emission lines (e.g. Fan et al. 1999; Diamond-Stanic et al. 2009; Plotkin et al. 2010). They have Ly α +N V rest-frame equivalent widths (REWs) $\lesssim 15$ Å and/or C IV REWs $\lesssim 10$ Å; these numbers represent $\gtrsim 3\sigma$ negative deviations from the REW distribution means with no corresponding positive “tail” to the distribution. Their C IV and other high-ionization lines also often show remarkably large blueshifts of ≈ 2000 –10000 km s⁻¹ (e.g. Wu et al. 2011, 2012; Luo et al. 2015, hereafter Wu11; Wu12; Luo15). The majority of these weak-line quasars (WLQs) are radio quiet and are *not* BL Lacs (e.g. Wu11; Wu12; Luo15). Multi-

* E-mail: qxn1@psu.edu

wavelength and multi-epoch studies also argue strongly that the weakness of the lines is not caused by line obscuration, gravitational lensing or microlensing effects, broad absorption line (BAL) effects, or radiatively inefficient accretion flows (e.g. [Diamond-Stanic et al. 2009](#); [Shemmer et al. 2010](#); [Lane et al. 2011](#); [Wu11](#); [Wu12](#); [Luo15](#); [Plotkin et al. 2015](#)). The fraction of WLQs among quasars also appears to rise with redshift (e.g. [Diamond-Stanic et al. 2009](#); [Luo et al. 2015](#); [Bañados et al. 2016](#)), perhaps due to generally higher Eddington ratios (L/L_{Edd}) at high redshift (e.g. [Shen & Kelly 2012](#)).

Investigations of the basic X-ray properties of WLQs have found them to be remarkable objects (e.g. [Wu11](#); [Wu12](#); [Luo15](#)). First, about half of the WLQ population shows notably weak X-ray emission (by an average factor of ≈ 20) compared to expectations from their optical/UV continuum emission (i.e., considering α_{OX} and $\Delta\alpha_{\text{OX}}$).¹ This X-ray weakness is further confirmed by examination of the broadband spectral energy distributions (SEDs) of WLQs (e.g. see Section 4.2 of [Luo15](#)). The fraction of X-ray weak objects among WLQs appears to be much higher than that for the general quasar population ($\lesssim 8\%$ for $\Delta\alpha_{\text{OX}} < -0.2$, corresponding to an X-ray weakness factor > 3.3 ; e.g. [Gibson et al. 2008](#)), although quantification of this effect has been challenging owing to the strong selection effects in previous WLQ samples with sensitive X-ray coverage.

Stacking of the counts from the X-ray weak WLQs reveals that they have hard X-ray spectra, on average, with effective power-law photon indices of $\langle\Gamma\rangle \approx 1.4$ ([Luo15](#)). These hard X-ray spectra suggest that high levels of intrinsic X-ray absorption (with N_{H} of at least 10^{23} cm^{-2} , and perhaps much greater), Compton reflection, and/or scattering are commonly present, which is somewhat surprising given these quasars' typical blue UV/optical continua and broad, although weak, emission lines. The presence of such X-ray absorption, reflection, and/or scattering is further supported by a *Chandra* spectrum of SDSS J1521+5202, an extremely luminous WLQ showing $N_{\text{H}} \gtrsim 1.3 \times 10^{23} \text{ cm}^{-2}$ and allowing for Compton-reflection dominated spectral solutions where the column density is $N_{\text{H}} \gg 10^{24} \text{ cm}^{-2}$ ([Luo15](#)). Finally, the WLQs in the half of the population that is not X-ray weak show notably steep power-law spectra with $\langle\Gamma\rangle = 2.2 \pm 0.1$. Such steep power-law spectra generally indicate accretion at a high L/L_{Edd} (e.g. [Shemmer et al. 2008](#); [Risaliti et al. 2009](#); [Brightman et al. 2013](#)).

[Luo15](#) detailed a “shielding” model for WLQs that has the potential to explain, in a simple and unified manner, their weak UV lines, their remarkable X-ray properties, and their other multiwavelength properties (also see [Wu11](#), [Wu12](#)). To explain the weak UV lines, this model relies upon small-scale ($\lesssim 30R_{\text{S}}$, where R_{S} is the Schwarzschild radius of the central black hole) shielding of ionizing EUV/X-ray pho-

tons that prevents them from reaching the broad emission-line region (BELR). The shielding material is also responsible for the X-ray weakness/absorption seen in about half of WLQs; as discussed below, the absorption may be highly Compton thick with $N_{\text{H}} \gg 10^{24} \text{ cm}^{-2}$. When our line of sight intercepts the shield, we see an X-ray weak WLQ; when it misses the shield, we observe an X-ray normal WLQ. In both cases, ionizing EUV/X-ray photons produced on small scales are mostly prevented from reaching the (largely equatorial and unobscured) high-ionization BELR, thereby causing the weak high-ionization line emission. However, UV/optical photons produced on larger scales in the accretion disk remain always unobscured.

In the shielding model for WLQs, one must explain the nature of the putative shield—it must lie inside the BELR and be capable of blocking even high-energy X-rays. [Luo15](#) proposed that the shield may be the geometrically and optically thick inner accretion disk expected for a quasar accreting at a high Eddington ratio (e.g. [Abramowicz et al. 1988](#); [Jiang et al. 2014, 2018](#); [Sądowski et al. 2014](#); [Wang et al. 2014](#)). In Figure 1, we present a schematic illustration of this shielding model based on Figure 18 of [Luo15](#).² A high Eddington ratio is consistent with the steep power-law X-ray spectra seen for X-ray normal WLQs as well as (admittedly uncertain) L/L_{Edd} estimates based on virial black-hole masses ([Luo15](#); [Plotkin et al. 2015](#)). High L/L_{Edd} values are also consistent with arguments that the Eddington ratios of quasars generally increase with declining C IV REWs and rising C IV blueshifts (e.g. [Shen & Ho 2014](#); [Sulentic et al. 2014](#); [Shemmer & Lieber 2015](#); [Sun et al. 2018](#)). We note that the thick disks associated with high L/L_{Edd} accretion are expected to have substantial associated outflows (e.g. [Jiang et al. 2014, 2018](#); [Dai et al. 2018](#)), and these likely also contribute to the shielding (e.g. [Wu11](#); [Wu12](#)). However, the detailed nature of these outflows remains uncertain. For this reason, as well as the purpose of simplicity, throughout we will just refer to the “thick disk” as the shield, and we implicitly include any associated outflow within this term.

The continuity of the quasar population in the C IV REW vs. C IV blueshift plane, as well as semi-analytic models and numerical simulations (e.g. [Sądowski 2009, 2011](#); [Jiang et al. 2014, 2018](#)), suggest that if a thick inner accretion disk is present in these extreme WLQs with high Eddington ratios, then it is also likely present, albeit with a lower height (and thus covering factor), in quasars with lower L/L_{Edd} . Thus, shielding by inner disks may play a broader role, beyond just extreme WLQs, in regulating the high-ionization emission-line strengths of quasars (e.g. [Leighly 2004](#); [Luo15](#)). As L/L_{Edd} continuously declines within a sample of quasars, shielding may also drop due to a reduction in the thickness of the inner accretion disk allowing the production of generally stronger emission lines. Of course, other factors are also expected to influence emission-line strengths,

¹ α_{OX} is the power-law slope connecting the monochromatic luminosities at rest-frame 2500 Å and 2 keV; i.e., $\alpha_{\text{OX}} = 0.3838 \log(L_{2 \text{ keV}}/L_{2500 \text{ Å}})$. This parameter is found to be correlated with $L_{2500 \text{ Å}}$ (e.g. [Wilkes et al. 1994](#); [Vignali et al. 2003](#); [Strateva et al. 2005](#); [Steffen et al. 2006](#); [Just et al. 2007](#); [Lusso et al. 2010](#)). We also define $\Delta\alpha_{\text{OX}} = \alpha_{\text{OX}}(\text{Observed}) - \alpha_{\text{OX}}(L_{2500 \text{ Å}})$, which quantifies the deviation of the observed X-ray luminosity relative to that expected from the $\alpha_{\text{OX}}-L_{2500 \text{ Å}}$ relation. $\Delta\alpha_{\text{OX}}$ is used to derive the stated factors of X-ray weakness.

² Our schematic in Figure 1 differs from that in [Luo15](#) in the disk profile, the inclusion of the outflow, and the location of the BELR. These changes have been made to reflect current thinking about super-Eddington accretion disks (e.g. S. Davis & Y. Jiang 2015, personal communication; [Sądowski et al. 2015](#); [Jiang et al. 2018](#)), in which optically thick outflows are expected and the radius at which the disk approaches a geometrically thin standard disk may be substantially larger than assumed in [Luo15](#).

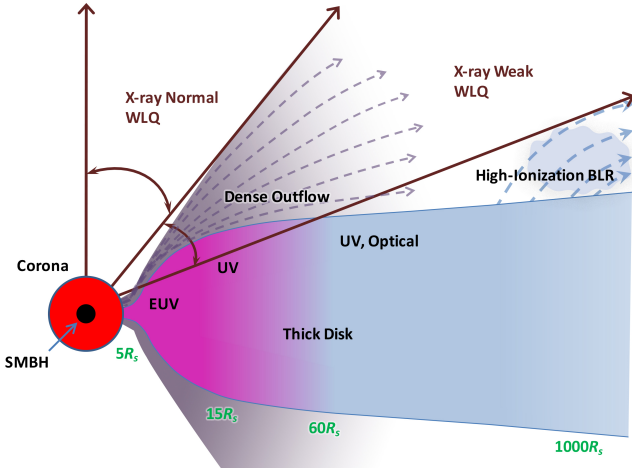


Figure 1. Schematic diagram of the geometrically thick-disk scenario for WLQs. The height of the disk increases with the Eddington ratio. The geometrically thick disk (as well as the associated dense outflow) expected for a quasar accreting at high Eddington ratio prevents the nuclear ionizing photons from reaching the high-ionization BELR, leading to the observed weak high-ionization line emission. The observed X-ray weakness occurs when our line of sight happens to intercept the thick disk. The approximate radial scale of the disk is annotated in units of the Schwarzschild radius (R_s); the vertical extent of the disk beyond the outward flare of the profile at 5–15 R_s is only shown schematically.

including gas metallicity and anisotropic line emission. Due to object-to-object differences in these secondary factors, correlations between L/L_{Edd} and emission-line strengths are expected to have intrinsic scatter (e.g. [Shemmer & Lieber 2015](#)).

While the above discussion has focused on the shielding model for WLQs, other explanations for their properties have also been put forward. These include an anemic BELR (e.g. [Shemmer et al. 2010](#)), a still-developing BELR (e.g. [Hryniewicz et al. 2010](#)), and a “soft” ionizing continuum arising from the relatively low-temperature accretion disk of an extremely massive black hole (e.g. [Laor & Davis 2011](#)). While these explanations for WLQs have some attractive aspects, they cannot compellingly account for the more recently established notable X-ray properties of WLQs described above—the shielding model was designed to explain both the observed X-ray and optical/UV properties of WLQs. Furthermore, we note that the [Luo15](#) stacking-based measurements of X-ray properties can only constrain these properties on average, and it is possible that there are some intrinsically X-ray weak objects among WLQs as well; i.e., quasars where the central engine simply fails to generate X-rays at the nominal level. Such WLQs would be similar to the well-studied intrinsically X-ray weak quasar PHL 1811 (e.g. [Leighly et al. 2007](#)), and the shielding model would likely not be applicable for them. [Luo15](#) provide further discussion on the possibility of some intrinsically X-ray weak objects among the WLQs, though due to relatively weak X-ray upper limits for many individual objects this issue remains poorly understood.

1.2 Motivation for the current study

Our initial investigations of the nature of WLQs via X-ray observations primarily utilized brief exploratory *Chandra* observations of the most-extreme WLQs—we were attempting to define the basic X-ray nature of these exceptional and poorly understood objects rather than observing well-defined, representative samples. For example, we preferentially targeted WLQs with the weakest possible C IV lines or those selected to have other exceptional properties, such as strong UV Fe II/Fe III emission and large C IV blueshifts (see, e.g. [Luo15](#) for details). While this approach was successful for gaining the basic understanding described above, it obviously has limitations. For example, the complex underlying selection effects prevented proper assessment of if/how the fraction of X-ray weak objects depends upon C IV REW. Such a dependence would be of considerable physical interest since, as described in Section 1.1, the shielding model predicts a decline in this fraction with rising C IV REW—the predicted decline thus offers one test of the shielding model. Indeed, if confirmed, the strength and form of this reduction should provide insight into how the covering factor of the shielding material regulates C IV line production.

Previously, we only had a small representative sample of WLQs with X-ray coverage for C IV REW values of $\lesssim 5 \text{ \AA}$. This sample was based on the WLQs originally identified by [Plotkin et al. \(2010\)](#), and it was completely disjoint from the main population of typical quasars which mostly have C IV REW = 15–100 \AA (see Figure 2). We therefore proposed in *Chandra* Cycle 17 to observe a sample of 14 quasars with C IV REW values ≈ 5 –15 \AA , aiming to build an unbiased X-ray observational “bridge” between the [Plotkin et al. \(2010\)](#) WLQs and more typical quasars. With these additional data in hand, one of our primary goals is to perform assessments of the fraction of quasars that are X-ray weak over the broad C IV REW range of ≈ 3 –100 \AA .

In addition to studying the fraction of quasars that are X-ray weak as a function of C IV REW, we furthermore desire to improve understanding of likely connections between UV continuum/emission-line properties and X-ray weakness. [Luo15](#) reported that red UV continuum color [e.g. measured with $\Delta(g-i)$] and large 2250–2650 \AA Fe II REW empirically appear to serve as effective tracers of X-ray weakness among WLQs. These were not the tracers we had expected, and we are still attempting to understand why they work as well as they apparently do. Mild intrinsic reddening in the equatorial plane (e.g. [Elvis 2012](#)) and aspect-dependent accretion-disk emission may be relevant; see §5 and §6 of [Luo15](#). However, the complex underlying selection effects and small size of our current WLQ sample limit the analyses of such tracers. The new X-ray observations presented here should aid in establishing which UV continuum/emission-line properties are indeed most closely linked to X-ray weakness, so that interpretation of these connections can proceed with confidence.

1.3 Paper layout and defined quantities

The layout of this paper is as follows. We describe the sample selection and X-ray data analysis in Sections 2 and 3. Multiwavelength analyses, including studies of $\Delta\alpha_{\text{OX}}$, UV emission-line properties, infrared to X-ray SEDs, and ra-

dio properties are given in Section 4. The likely absorption nature of X-ray weakness is demonstrated in Section 5.1. Changes in the fraction of X-ray weak quasars with high-ionization emission-line strength are presented in Section 5.2, and possible UV continuum/emission-line tracers of X-ray weakness are discussed in Section 5.3.

Throughout this paper, we use J2000 coordinates and a cosmology with $H_0 = 67.8 \text{ km s}^{-1} \text{ Mpc}^{-1}$, $\Omega_M = 0.308$, and $\Omega_\Lambda = 0.692$ (Planck Collaboration et al. 2016).

2 SAMPLE SELECTION AND CHANDRA OBSERVATIONS

We have selected 32 representative WLQs with C IV REW $\lesssim 15 \text{ \AA}$ to investigate the nature of X-ray weakness with reduced selection bias compared to our previous work. Fourteen of them were proposed and observed by *Chandra* in Cycle 17, and the remaining 18 have archival X-ray observations (see Sections 2.1 and 2.2 for details). These 32 WLQs are divided into two subsamples, the “bridge subsample” and the “extreme subsample”, according to their C IV REW (see Section 2.2), for study purposes. In addition, a larger sample of 63 WLQs, though not as consistently selected, is utilized to help probe potential tracers of X-ray weakness (see Section 2.3). Two subsamples of the Gibson et al. (2008) Sample B quasars are utilized (see Section 2.2) as well for sample comparisons. All the samples we utilized for this paper are summarized in Table 1.

2.1 Target selection and Chandra observations

Since typical quasars have C IV REW $\approx 15\text{--}100 \text{ \AA}$ and WLQs with C IV REW $\lesssim 5 \text{ \AA}$ have been well-observed in the X-ray band in recent years, our targeted *Chandra* Cycle 17 WLQs have been selected from radio-quiet ($R < 10$) quasars in the SDSS Data Release 7 (DR7) quasar properties catalog (Shen et al. 2011) with C IV REW = $5\text{--}15 \text{ \AA}$ (which bridges the gap between previously X-ray observed extreme WLQs and typical quasars). We also require $m_i \leq 18.2$, which is optically bright enough to allow economical snapshot *Chandra* observations, and $1.7 < z < 2.2$, in order to have spectral coverage from Si IV to Mg II. Objects with narrow absorption features around C IV, BAL or mini-BAL features, or very red spectra with $\Delta(g-i) > 0.45$ were excluded since we want to avoid any potentially confusing X-ray absorption associated with, e.g. quasar winds.

Among the 20 selected quasars, four objects have already been targeted by *Chandra* (SDSS J082508.75+115536.3, SDSS J132809.59+545452.7, and SDSS J153913.47+395423.4 were targeted in *Chandra* Cycle 14; SDSS J215954.45-002150.1 was targeted in Cycle 11). Two further objects have been recorded in X-ray survey catalogs: SDSS J113949.39+460012.9 in the full *XMM-Newton* slew-survey catalog (Saxton et al. 2008) and SDSS J123326.03+451223.0 in the *ROSAT* all-sky survey catalog (Boller et al. 2016). The relevant two X-ray survey sources match the quasar positions to within (relatively large) positional uncertainties, and we do not find other likely optical counterparts for them. Thus, we take these two quasars to be X-ray detected, although ideally we would

prefer more secure identifications. This left 14 objects for *Chandra* observation.

Our *Chandra* observations were performed between 2015 Dec 28 and 2016 Aug 15 using the Advanced CCD Imaging Spectrometer spectroscopic array (ACIS-S) (Garmire et al. 2003) with VFAINT mode. The exposure times of our targets range from 3.1 to 4.8 ks. Table 2 lists details of these 14 observations.

2.2 Bridge WLQs vs. extreme WLQs in the representative sample

As we have previously mentioned, WLQs with C IV REW $\lesssim 5 \text{ \AA}$ have been targeted in X-rays and studied in detail because of their extreme properties.

In order to assemble an unbiased, statistically representative sample of WLQs with C IV REW $\lesssim 5 \text{ \AA}$, we select ten WLQs from the Plotkin et al. (2010) catalog, which identified WLQs from the full SDSS DR7 spectroscopic database as quasars having C IV REW $\lesssim 5 \text{ \AA}$. We used the same criteria as those in Section 2.1 except for the m_i and redshift requirements. An i -band magnitude of $m_i < 18.6$ is applied, and a redshift satisfying $1.5 < z < 2.5$ is required to have SDSS spectral coverage of the full C IV region (which has been the major selector for weak emission lines) and the 2250–2650 \AA Fe II region (which has been proposed as a UV tracer of X-ray weakness among WLQs). The differences among the selection criteria for m_i and redshift are small, and should not affect the results. All of the selected ten objects have archival X-ray observations available.

Besides these ten objects from the Plotkin et al. (2010) catalog, we also include two additional WLQs with X-ray observations: SDSS J094533.98+100950.1, identified by Hryniewicz et al. (2010), and SDSS J090312.22+070832.4, identified by Wu11, satisfying the same criteria for radio loudness, C IV REW, and redshift.

Together with the 20 WLQs with C IV REW = $5\text{--}15 \text{ \AA}$ selected in Section 2.1, we have 32 (20+12) WLQs in total. According to the “shielding” model of Section 1.1, we expect WLQs that are more heavily shielded (thus having weaker high-ionization UV emission-line strengths) as a result of thicker disks to be more inclined to be X-ray weak.

Thus, we divided the 32 selected WLQs in the representative sample into two subsamples with equal numbers of objects according to their consistently re-measured C IV REW (see Section 4.3) in order to achieve the maximum statistical power in sample comparisons—this requirement leads to a subsample division threshold of 7 \AA . Sixteen WLQs with C IV REW $< 7.0 \text{ \AA}$ are classified as the “extreme subsample”, while 16 WLQs with C IV REW = $7.0\text{--}15.5 \text{ \AA}$ are classified as the “bridge subsample”. We only list archival X-ray observations of WLQs that have not yet been analyzed/published in Table 2 along with *Chandra* Cycle 17 observations of targeted WLQs.

Figure 2 compares the C IV REWs and blueshifts (as measured in Section 4.3) of the objects in the extreme and bridge subsamples to those of typical radio-quiet quasars. The latter include quasars from Richards et al. (2011) and two subsamples of the Gibson et al. (2008) Sample B

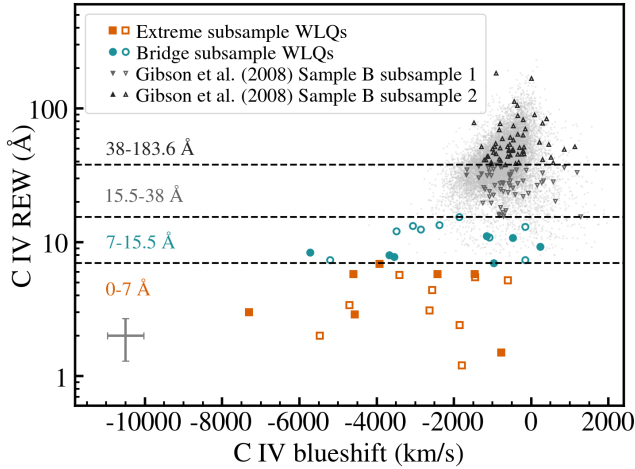


Figure 2. C IV REW vs. C IV blueshift. The extreme subsample, the bridge subsample, and two subsamples of the Gibson et al. (2008) Sample B quasars are distinguished using symbol types as labeled. Solid symbols indicate X-ray weak WLQs, while open symbols indicate X-ray normal WLQs. The median uncertainties of C IV REW and C IV blueshift for WLQs are shown as the gray error bars in the bottom-left corner of the plot, and account for only the dominant error factors; i.e., the measurement error. The dashed lines represent the C IV REW division lines between the four subsamples, and the C IV REW ranges of the four subsamples are labeled. 13582 typical radio-quiet quasars in Richards et al. (2011) are represented by the gray dots in the background.

quasars.³ The Gibson et al. (2008) Sample B quasars represent typical SDSS quasars that are radio-quiet ($R < 10$) and lack BALs, which are also the selection requirements of our representative sample. All the quasars in the Gibson et al. (2008) Sample B have quality X-ray observations available, making comparisons of X-ray properties with our representative sample possible. In this paper, two subsamples of the Gibson et al. (2008) Sample B quasars are utilized; they are divided according to their C IV REW, one set with $15.5 \text{ \AA} < \text{C IV REW} < 38.0 \text{ \AA}$ and the other with $\text{C IV REW} \geq 38.0 \text{ \AA}$, with nearly equal size (59/60) to achieve the maximum statistical power in sample comparisons. They also have comparable redshift ranges ($1.7 < z < 2.7$) with our representative sample (see Table 1 and Figure 3).

Though selected only by C IV REWs, we can also see the increasing trend in the C IV blueshift values of the 32 selected WLQs when comparing with typical quasars or within the representative sample. The Eddington ratios of quasars generally increase as we move in Figure 2 toward small C IV REW and large C IV blueshift (e.g. Richards et al. 2011; Shen

³ We utilized an “ultra clean” version of the Gibson et al. (2008) Sample B of radio-quiet, non-BAL quasars, where seven likely BAL quasars and six likely mini-BAL quasars were removed as a result of the revision of the continuum model or the C IV emission-line profile (see Footnote 16 of Wu11). Four objects with $\Delta(g-i) > 0.45$ (J1002+0203, J1245-0021, J1452+5804, and J1618+3456) were also removed (J1245-0021 and J1618+3456 are also likely mini-BAL quasars) to maintain consistency with the representative sample.

& Ho 2014; Sulentic et al. 2014; Sun et al. 2018), and quasars accreting with high Eddington ratios are expected to have geometrically thick inner accretion disks (e.g. Abramowicz et al. 1988; Jiang et al. 2014, 2018; Sądowski et al. 2014; Wang et al. 2014). Thus, among our selected WLQs, we plausibly expect the presence of thick inner disks that can block ionizing photons from reaching the high-ionization BELR. These thick inner disks could also cause X-ray weakness when oriented such that they block our line-of-sight to the compact X-ray emission region (see Figure 1).

2.3 Full sample

In addition to performing analyses with the representative sample, we also utilize a larger “full sample”. This sample is not as uniformly defined and unbiased as the representative sample, but its larger size makes it useful to improve the significance of our study and further assess the results obtained from the representative sample, especially when investigating UV tracers of X-ray weakness.

There are 63 WLQs in our full sample. Besides the 32 WLQs in the representative sample, we also add 31 WLQs with X-ray measurements that do not have BAL features or very red spectra: 19 from Luo15, 6 from Wu11, and 6 from Wu12.

These quasars were originally targeted with rather complex selection rules for the X-ray observations. Some of these objects have redshift values either too high or too low to allow spectral coverage of the full C IV and Fe II regions. Some were targeted when studying “PHL 1811 analogs”; additional requirements on Fe II/Fe III strength and C IV blueshift rendered them not ideal objects to include in the representative sample for an unbiased study.

Figure 3 displays the redshift vs. absolute i -band magnitude plot of all the objects in the full sample. In comparison with the full sample, the representative sample is selected in a narrower redshift range.

3 X-RAY PHOTOMETRIC ANALYSIS

We processed the *Chandra* Cycle 17 data using the Chandra Interactive Analysis of Observations (CIAO) tools (Fruscione et al. 2006). The CHANDRA_REPRO script was employed for the latest calibration. The DEFLARE script was used to remove background flares with sigma clipping at a 3σ level. The final exposure times for each quasar are listed in Table 2.

We produced images for each source in the 0.5–2 keV (soft), 2–8 keV (hard), and 0.5–8 keV (full) bands from the cleaned event file using the standard *ASCA* grade set (0, 2, 3, 4, 6). WAVDETECT with a $\sqrt{2}$ sequence of wavelet scales (1, 1.414, 2, 2.828 and 4 pixels) was run in each band to find X-ray sources with a false-positive probability threshold of 10^{-6} .

If we detect a source in no fewer than one band, the WAVDETECT position which is closest to the SDSS position is adopted as the source position. If WAVDETECT does not successfully identify any source, the SDSS position is adopted as the X-ray position. We also ensure that no confusion has been made with source identifications (e.g. no other potential close sources). The X-ray-to-optical offsets

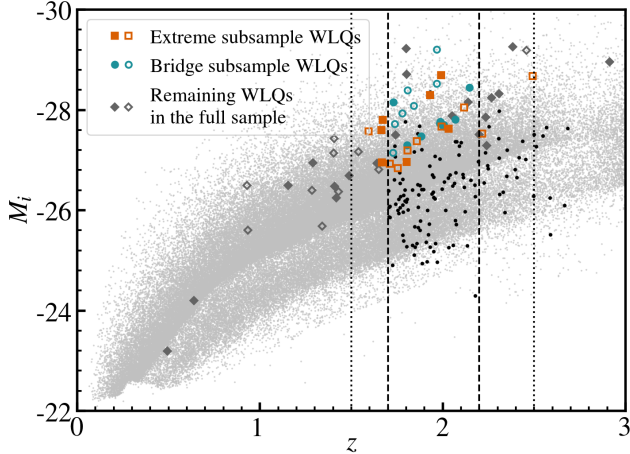


Figure 3. Redshift vs. absolute *i*-band magnitude of the 63 WLQs in the full sample. Squares and circles represent WLQs in the representative sample, and the diamonds indicate the remaining WLQs. Solid symbols depict X-ray weak WLQs, while open symbols depict X-ray normal WLQs. The gray dots in the background indicate objects from the SDSS DR7 quasar catalog (Schneider et al. 2010), and the black dots in the background indicate quasars from Gibson et al. (2008) Sample B. The vertical dashed lines show the narrow redshift spread for the bridge subsample, and the vertical dotted lines show the redshift spread for the extreme subsample.

for the detected sources have a mean value of $0.54''$, consistent with expectations.

Aperture photometry is performed in both the soft band and hard band, following the approach of Luo15. For all the objects, we extracted source counts from a circular aperture with radius $2''$ centered on the source position, which corresponds to encircled-energy fractions of 0.959 in the soft band and 0.907 in the hard band. We extract background counts from source-free annular regions with an inner radius of $10''$ and an outer radius of $40''$.

In order to determine the significance of the source signal, a binomial no-source probability (the probability of detecting the source counts by chance when there is no real source), P_B (e.g. Broos et al. 2007; Xue et al. 2011; Luo et al. 2013, 2015), is computed for each band for each object; P_B is defined as:

$$P_B(X \geq S) = \sum_{x=S}^N \frac{N!}{x!(N-x)!} p^x (1-p)^{N-x}$$

In this equation, S represents the number of counts in the source area, B represents the number of counts in the background area, and $N = S + B$. $p = 1/(1 + \text{BACKSCAL})$, where BACKSCAL is the ratio of background-extraction area to source-extraction area.

When the calculated P_B value is no more than 0.01, we consider the source to be detected in this band. This threshold is appropriate given that we are checking for detections only at pre-specified positions. The 1σ errors of the source counts and background counts were obtained following Gehrels (1986). We followed Section 1.7.3 of Lyons (1991) to calculate the 1σ error of net counts. When $P_B > 0.01$, the source is considered to be undetected in this band.

The upper limits on the source counts for such cases were derived using the 90% confidence-level table in Kraft et al. (1991). The results from the above calculations are presented in Table 2.

The ratio of hard-band counts to soft-band counts is defined as the band ratio. The band ratio and its uncertainty (for sources detected in both bands) or upper limit (for sources only detected in the soft band) were obtained from the Bayesian Estimation of Hardness Ratios code BEHR (Park et al. 2006). The 0.5–8 keV effective power-law photon index (Γ_{eff}) or its lower limit for each source was derived from the band ratio using the CIAO script MODELFLUX, adopting a power-law spectrum with Galactic absorption. When sources are undetected in both the soft and hard bands, we are unable to place any constraints on Γ_{eff} . Since luminous radio-quiet quasars typically have $\Gamma_{\text{eff}} = 1.8 - 2.0$ (e.g. Reeves et al. 1997; Just et al. 2007; Scott et al. 2011), we adopt $\Gamma_{\text{eff}} = 1.9$ for the flux calculation of undetected sources. If such sources appear to be X-ray weak (as defined in Section 4.1) after the first calculation, their X-ray properties are recalculated with $\Gamma_{\text{eff}} = 1.4$, which is the Γ_{eff} value from X-ray stacking results for 30 X-ray weak WLQs in Luo15.

4 MULTIWAVELENGTH ANALYSES

4.1 X-ray to optical properties

We measured the X-ray to optical power-law slope value (α_{OX}) for our *Chandra* Cycle 17 sample objects and the archival objects that had not been previously analyzed, which was calculated from the rest frame 2500 Å and 2 keV flux densities (see Footnote 1 for details).

The rest-frame 2500 Å flux densities were taken from the Shen et al. (2011) SDSS DR7 quasar properties catalog. By assuming a power-law spectrum modified by Galactic absorption (see Section 3 for the process of deriving Γ_{eff}), we can derive the unabsorbed soft-band (0.5–2 keV) flux (which covers 2 keV in the rest frame for all our sources) from the net count rate in the soft band using MODELFLUX, and thus calculate the rest-frame 2 keV flux densities. If we did not detect a source in the soft band, we could get an upper limit on $f_{2\text{keV}}$ following the same method using the upper limit for the soft-band net count rate. The flux densities and the calculated α_{OX} values are listed in Table 3.

One can derive an expected value of α_{OX} , $\alpha_{\text{OX}}(L_{2500 \text{ Å}})$, from the empirical $\alpha_{\text{OX}}-L_{2500 \text{ Å}}$ relation (e.g. Just et al. 2007) for typical optically-selected quasars. The difference between the observed α_{OX} and the expected value $\alpha_{\text{OX}}(L_{2500 \text{ Å}})$, $\Delta\alpha_{\text{OX}} = \alpha_{\text{OX}}(\text{Observed}) - \alpha_{\text{OX}}(L_{2500 \text{ Å}})$, provides a basic measurement of X-ray weakness relative to the expected X-ray luminosity and a factor of X-ray weakness, f_{weak} . Sources with $\Delta\alpha_{\text{OX}} = -0.384$ have X-ray fluxes $\approx 10\%$ of those of typical quasars, so we define f_{weak} as $10^{-\Delta\alpha_{\text{OX}}/0.384}$, which is approximately $403^{-\Delta\alpha_{\text{OX}}}$.

The α_{OX} vs. $L_{2500 \text{ Å}}$ diagram for our representative sample is presented in Figure 4(a). Following Luo15, we use $\Delta\alpha_{\text{OX}} = -0.2$ ($f_{\text{weak}} = 3.3$) to separate X-ray weak quasars from X-ray normal quasars, which corresponds to the $\approx 90\%$ single-sided lower confidence limit of the expected α_{OX} distribution given the rms scatter in Steffen et al. (2006). A large fraction of our WLQs fall below this line, showing

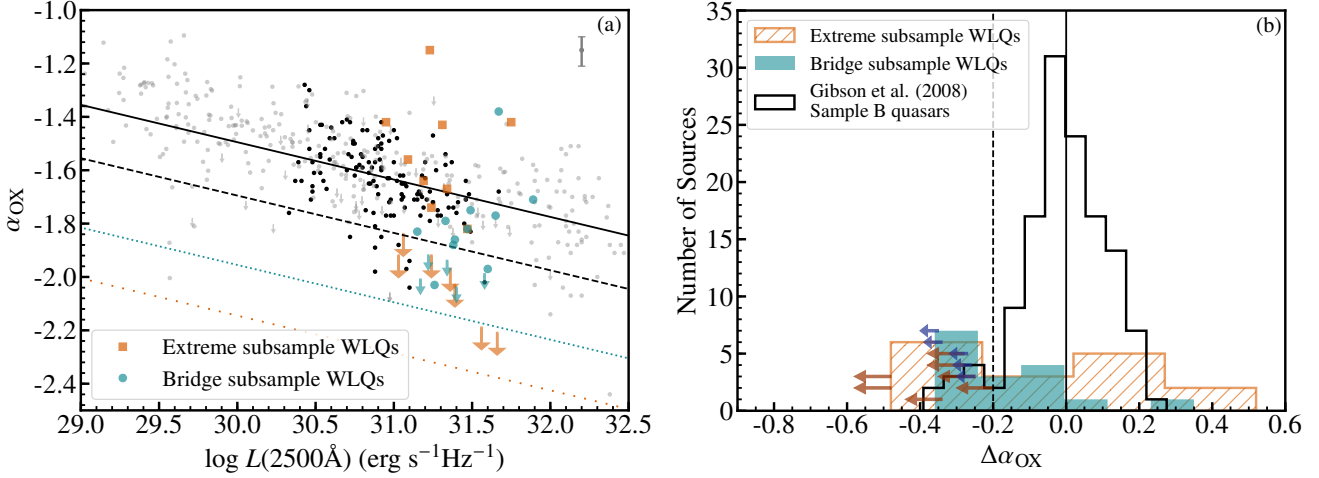


Figure 4. (a). X-ray-to-optical power-law slope (α_{OX}) vs. 2500 Å monochromatic luminosity for the bridge subsample WLQs (circles) and extreme subsample WLQs (squares). In cases of X-ray non-detections, the 90% confidence upper limits of α_{OX} for extreme/bridge WLQs are represented by the downward long/short arrows. For comparison, Gibson et al. (2008) Sample B quasars are indicated by the black dots, and quasars from Steffen et al. (2006) and Just et al. (2007) are indicated by the gray dots and downward arrows, representing upper limits. The median measurement error of α_{OX} (estimated from the count-rate uncertainty) for detected WLQs is represented by the gray error bar in the upper-right corner of the plot, while the measurement error of $L_{2500\text{\AA}}$ (≈ 0.01 dex) is too small to be shown in the plot. The solid line stands for the $\alpha_{\text{OX}}-L_{2500\text{\AA}}$ relation from Just et al. (2007); the dashed line ($\Delta\alpha_{\text{OX}} = -0.2$) represents the adopted division between X-ray normal and X-ray weak quasars in this study. The blue dotted line ($\Delta\alpha_{\text{OX}} = -0.46$) marks the stacked mean of X-ray weak WLQs in the bridge subsample, while the orange dotted line ($\Delta\alpha_{\text{OX}} = -0.65$) marks the stacked upper limit of X-ray weak WLQs in the extreme subsample (see Section 4.2 below). (b). Distribution of $\Delta\alpha_{\text{OX}}$ values. The solid histogram represents sources in the bridge subsample, while the hatched histogram represents sources in the extreme subsample. The histogram bin widths are decided by Knuth’s rule (Knuth 2006). The short and long arrows distinguish WLQs in the bridge and extreme subsamples for which the $\Delta\alpha_{\text{OX}}$ value counted in the histogram is only an upper limit at the 90% confidence level. The unshaded histogram represents the $\Delta\alpha_{\text{OX}}$ distribution for the Gibson et al. (2008) Sample B quasars, which is plotted for comparison. The vertical dashed line (at $\Delta\alpha_{\text{OX}} = -0.2$) represents the adopted threshold for defining X-ray weakness in this study.

X-ray weakness. The distributions of $\Delta\alpha_{\text{OX}}$ for the extreme subsample and bridge subsample are shown in Figure 4(b) and compared with the typical quasar distribution from the Gibson et al. (2008) Sample B quasars.

4.2 X-ray stacking analyses of WLQs

The limited number of counts for each X-ray weak WLQ has prevented us from carrying out individual X-ray spectral analyses, but we could probe the average spectral properties of the population with stacking. We performed the X-ray stacking analyses by adding the extracted source and background counts of objects together and carried out the same X-ray photometric analyses as in Section 3 for X-ray weak WLQs in the extreme subsample, the bridge subsample, and the whole representative sample. The results of this exercise are given in Table 4.

X-ray weak WLQs in the whole representative sample have a stacked power-law effective photon index of $\Gamma_{\text{eff}} = 1.19^{+0.56}_{-0.45}$. While Γ_{eff} could not be constrained for X-ray weak WLQs in the extreme subsample due to the limited number of photons detected, the X-ray weak WLQs in the bridge subsample have a stacked $\Gamma_{\text{eff}} = 1.09^{+0.55}_{-0.45}$. This result justifies our choice of $\Gamma_{\text{eff}} = 1.4$ when performing X-ray photometric analysis; i.e., X-ray weak WLQs have harder Γ_{eff} compared with typical luminous radio-quiet quasars, which have $\Gamma \approx 1.9$ (see Section 3). This result also provides support to our shielding model by suggesting high levels of intrinsic X-ray absorption, Compton reflection, and/or scattering,

which are reflected by hard spectral shapes (see Section 5.1 for further discussion).

Table 4 also shows that the stacked $\Delta\alpha_{\text{OX}}$ value of X-ray weak WLQs is -0.45 ± 0.11 for the bridge sample (the error is calculated via bootstrapping source counts), and only an upper limit of -0.64 could be obtained for the extreme sample.

4.3 UV emission-line measurements

Since some UV emission-line properties are considered to be potential tracers of X-ray weakness, we performed emission-line measurements for the objects in the bridge subsample based on their SDSS spectra. The SDSS spectra of these WLQs are shown in Figure 5, compared with the SDSS quasar composite spectrum from Vanden Berk et al. (2001). Most of the WLQs in the extreme subsample were previously measured in Luo15, and our *Chandra* Cycle 17 targets making up the bridge subsample were analyzed in the same manner.

The UV emission-line properties listed in Table 5 were measured following the methods in Section 2.2 of Wu11 and Section 2.3 of Luo15, with the Hewett & Wild (2010) redshift adopted. The wavelength-fitting regions of the subtracted local power-law continuum for the Si IV $\lambda 1397$, C IV $\lambda 1549$, $\lambda 1900$ complex (mainly C III] $\lambda 1909$), Fe III UV48 $\lambda 2080$, and Mg II $\lambda 2799$ emission features are taken from Table 2 of Vanden Berk et al. (2001). The UV Fe II was fitted between 2250 Å and 2650 Å, following Luo15.

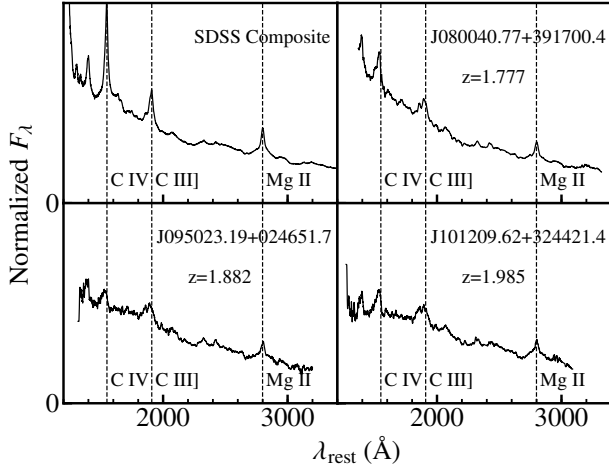


Figure 5. SDSS spectra of WLQs in the bridge subsample. A full version of this figure with all the spectra presented following the order of WLQs in Table 5 is available in the online version. The flux density in arbitrary linear units is plotted on the y-axis. Dereddening and smoothing (with a 20-pixel boxcar) have been applied for each spectrum. In the upper left panel, the composite spectrum of SDSS quasars from Vanden Berk et al. (2001) is presented for comparison.

4.4 Infrared-to-X-ray SEDs

The infrared (IR) to X-ray continuum SEDs for the bridge WLQ and the extreme WLQ subsamples were constructed with photometric data from the *Wide-field Infrared Survey Explorer* (*WISE*; Wright et al. 2010), Two Micron All Sky Survey (2MASS; Skrutskie et al. 2006), SDSS, *Galaxy Evolution Explorer* (*GALEX*; Martin et al. 2005), and *Chandra*.

WISE measured our targets at 3.4, 4.6, 12, and 22 μm . We convert *WISE* magnitudes of our sources to flux densities following the method of Wright et al. (2010). 2MASS measured targets in the *J*, *H*, and *K_s* bands, and we convert the magnitudes to flux densities following Cohen et al. (2003). *GALEX* measured AB magnitudes in the FUV band (1350–1750 Å) and NUV band (1750–2750 Å). We applied the dereddening method in Cardelli et al. (1989) and O’Donnell (1994) to correct for the Galactic extinction.

Figure 6 displays the combined SEDs of the 16 WLQs in the bridge subsample and the 16 WLQs in the extreme subsample. The composite SED of optically luminous SDSS quasars from Richards et al. (2006) is included for comparison. All the WLQs in the representative sample have IR-to-UV SEDs similar to those of typical quasars, which further eliminates the possibility of contamination from BL Lacs (e.g. Lane et al. 2011). This similarity also justifies that our calculation of $\Delta\alpha_{\text{OX}}$, the observed deviation from the expectation value of the X-ray to optical power-law slope, is valid for probing the degree of X-ray weakness, since it is not affected by any anomaly in optical properties.

4.5 Radio properties

We only include radio-quiet ($R < 10$) quasars in samples used in this study. We computed the radio-loudness parameter as $R = f_{5 \text{ GHz}}/f_{4400 \text{ Å}}$ (e.g. Kellermann et al. 1989).

The rest-frame 5 GHz flux densities $f_{5 \text{ GHz}}$ were obtained by checking the Faint Images of the Radio Sky at Twenty-centimeters (FIRST) survey catalog (Becker et al. 1995; White et al. 1997) at the source position and converting the measured 1.4 GHz result to rest-frame 5 GHz with an assumed radio power-law index $\alpha_r = -0.5$ ($f_\nu \propto \nu^{\alpha_r}$; Kellermann et al. 1989). If sources were not detected by the FIRST survey, we obtained upper limits on the radio fluxes as $0.25 + 3\sigma_{\text{rms}}$ mJy, where 0.25 mJy stands for the CLEAN bias (White et al. 1997) and σ_{rms} represents the rms noise at the source position in the FIRST survey. The rest-frame 4400 Å flux densities were converted from the rest-frame 2500 Å flux densities, assuming an optical power-law slope of $\alpha_o = -0.5$ ($f_\nu \propto \nu^{\alpha_o}$; e.g. Richstone & Schmidt 1980; Vanden Berk et al. 2001). The calculated R values for bridge WLQs are listed in the last column of Table 3.

Among the 16 extreme WLQs, SDSS J084424.24+124546.5, SDSS J113949.39+460012.9, and SDSS J115637.02+184856.5 have point-like radio sources detected at the source positions. This is also the case for SDSS J123326.03+451223.0 and SDSS J215954.45–002150.1 among the 16 bridge WLQs. In all cases, these 5 objects are still radio quiet with $R = 2.8 - 8.0$, and a mean R of 5.0. We cannot completely exclude the possibility of some jet-linked X-ray contamination for these five objects (e.g. Miller et al. 2011), and they all proved to be X-ray normal WLQs with relatively high $\Delta\alpha_{\text{OX}}$. This behavior can also be seen clearly in Figure 6 where all these objects with radio detections (noted with black hexagons) show rest-frame 2 keV luminosities above the typical luminosities.

We have performed the same investigations as those on all the WLQs in the representative sample (see Section 5) for WLQs with no radio source detected, and we verify that our results are not materially influenced by including sources with radio detections. Thus, these WLQs are retained in the representative sample.

5 RESULTS AND DISCUSSION

5.1 The nature of X-ray weakness

In principle, a quasar can appear X-ray weak due to either X-ray absorption or intrinsic X-ray weakness (see Section 1.1 for further discussion). One important tool for discriminating between these two scenarios involves examination of X-ray spectral properties; e.g. a hard X-ray continuum shape, especially at high rest-frame energies, is generally indicative of a spectrum dominated by absorption, Compton reflection, and/or scattering. In this section, we therefore examine the X-ray spectral properties of our WLQ samples to the extent the data allow.

Power-law effective photon indices (Γ_{eff}) derived from band ratios are used to assess the X-ray continuum shape. Wu11, Wu12, and Luo15 all found relatively flat/hard effective power-law photon indices for their X-ray weak objects, suggesting heavy absorption.

The X-ray weak WLQs in our representative sample have a mean redshift of 1.884 (see Table 4), which is useful for probing the level of absorption since the X-ray fluxes in the rest frame are at relatively high energies ($\approx 2 - 23$ keV). However, only 1 out of 7 X-ray weak WLQs in the bridge

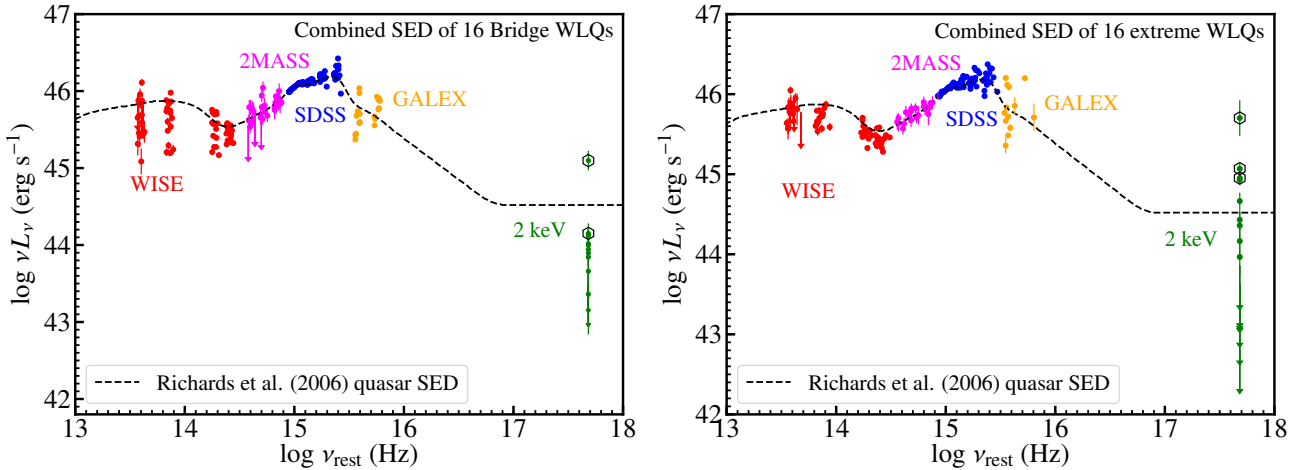


Figure 6. Combined SEDs of 16 WLQs in the bridge subsample (left) and 16 WLQs in the extreme subsample (right). The IR-to-UV SED data obtained from the *WISE*, 2MASS, SDSS, and *GALEX* catalogs are represented by red, magenta, blue, and orange points individually (the arrows represent 95% confidence upper limits for *WISE* and 2MASS data). The green data points and arrows represent luminosities and 90% confidence upper limits at 2 keV, and those with black hexagons indicate sources that were detected by FIRST. The SED of each WLQ was scaled at rest-frame 3000 Å (10^{15} Hz) to the composite SED (dashed line) of optically luminous quasars from Richards et al. (2006). (In the combined SEDs, we removed the data points collected from *GALEX* that are influenced by the Lyman break).

subsample has enough detected counts to constrain the Γ_{eff} , which is $0.9^{+0.5}_{-0.4}$ (see Table 2), and no X-ray weak WLQs in the extreme subsample has constrained Γ_{eff} (Wu11, Wu12, Luo15). Thus, we must rely on the results from X-ray stacking analyses (see Section 4.2) to probe the nature of X-ray weakness.

As shown in Table 4, all 14 X-ray weak WLQs in the representative sample have a stacked $\Gamma_{\text{eff}} = 1.19^{+0.56}_{-0.45}$, and the 7 X-ray weak WLQs in the bridge subsample have a stacked $\Gamma_{\text{eff}} = 1.09^{+0.55}_{-0.45}$. These numbers are consistent with the shielding model by showing the flatness of the spectrum compared with $\Gamma \approx 1.9$ expected in the case of typical luminous radio-quiet quasars (see Section 3). If an intrinsic $\Gamma \approx 1.9$ is assumed, $N_{\text{H}} \gtrsim 10^{23} \text{ cm}^{-2}$ is required to produce these stacked Γ_{eff} values at rest-frame 2–23 keV.

We caution that we cannot actually constrain the stacked Γ_{eff} for the extreme subsample, and the stacking results for the bridge subsample and the representative sample as a whole might be dominated by only a few sources. Thus, we cannot fully exclude the possibility that there might be some intrinsically X-ray weak quasars within our sample (also see Section 1.1). Nevertheless, the absorption scenario is still statistically preferred, which is consistent with the thick inner-disk model.

5.2 The fraction of X-ray weakness

Nearly half of the quasars (43.8%) in the whole representative WLQ sample are X-ray weak, which is a much larger fraction than reported for typical radio-quiet quasars in Gibson et al. (2008) Sample B (7.6%). Among the 16 bridge-subsample WLQs, 7 are X-ray weak, and the X-ray weak fraction is also 43.8%. For the extreme subsample, the number of X-ray weak quasars and the X-ray weak fraction are the same (see Table 6).

Assuming the binomial distribution, we use Table 1 of

Cameron (2011) to get the 1σ confidence intervals on the X-ray weak fractions, which are 32.7–56.2% for both the extreme and bridge subsamples. If sources with radio detections are removed from the representative sample, the X-ray weak fraction is 7/14 ($50.0^{+12.5}_{-12.5}\%$) among the bridge-subsample WLQs and 7/13 ($53.8^{+12.4}_{-13.4}\%$) among the extreme-subsample WLQs.

In order to investigate the dependence of the X-ray weak fraction upon the C IV REW more broadly, we have utilized the Gibson et al. (2008) Sample B quasars. We have used Fisher’s exact test (a contingency table test valid for all sample sizes) to compare the fractions of X-ray weak quasars among the extreme-subsample WLQs, the bridge-subsample WLQs, and the two Gibson et al. (2008) subsamples. Table 6 lists, for all subsample pairs, the results from Fisher’s exact test assessing the null hypothesis that the two subsamples have an equal fraction of X-ray weak quasars. Not all pairwise comparisons yield significant results. However, there is overall a highly significant trend showing a decline in the fraction of X-ray weak quasars with rising C IV REW. There is also an apparent trend of increasing median $\Delta\alpha_{\text{OX}}$ with rising C IV REW.

Figure 7(a) displays the X-ray weak fractions of the extreme and bridge subsamples of WLQs, together with those for the two Gibson et al. (2008) subsamples. The fraction of sources with $\Delta\alpha_{\text{OX}} \leq x$ for each of the four subsamples can be seen in Figure 7(b). The clear systematic decline in the X-ray weak fraction with increasing C IV REW is apparent. In the lightly shaded background of Figure 7(a), we also provide “running window” results. To derive these values, we combine the quasars in the four subsamples together, sort them by their C IV REW values, construct sets of quasars falling within a running window (which is stepped across the quasars with a step size of one quasar), and calculate the X-ray weak fraction and its 1σ confidence intervals for each window (using the same methodology as was used for

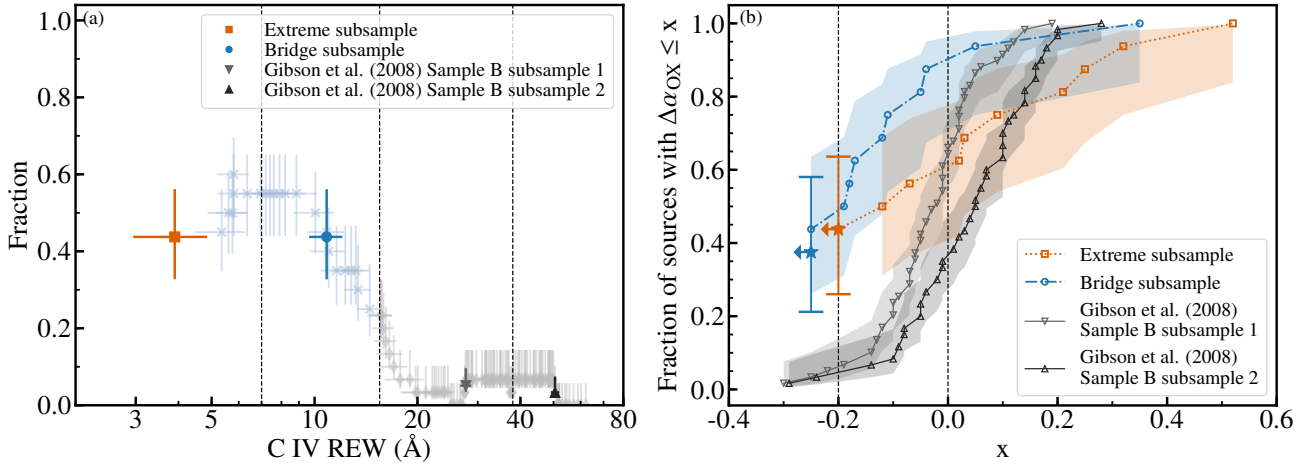


Figure 7. (a). The fraction of X-ray weak quasars vs. the C IV REW for the extreme subsample, bridge subsample, and two subsamples of the Gibson et al. (2008) Sample B quasars. The median C IV REW for each subsample is plotted with error bars calculated from bootstrap. The X-ray weak fraction for each subsample is displayed with 1σ error bars calculated from Cameron (2011). The vertical dashed lines mark the divisions of C IV REW between the four subsamples. The underlying lightly shaded crosses (thin diamonds) and their error bars represent the running-window results with a window size of 20 (30) objects using the four subsamples together. (b). The fraction of sources having $\Delta\alpha_{OX} \leq x$ vs. x for the extreme subsample, bridge subsample, and two subsamples of the Gibson et al. (2008) Sample B quasars. For $\Delta\alpha_{OX}$ below the measured value closest to the position of the star (which is the highest upper limit of $\Delta\alpha_{OX}$ we obtained for individual sources in the subsample), we could not constrain the relevant fraction. The shaded regions (and the error bars attached to the stars) represent the 90% confidence intervals for the fractions, calculated following Cameron (2011).

the four subsamples). The adopted width of the running window is 20 quasars for C IV REW $< 15 \text{ \AA}$ and 30 quasars for higher C IV REW. The running-window results also clearly show the systematic drop in the X-ray weak fraction with increasing C IV REW, providing a more continuous view of this trend. The drop is especially pronounced in the 10–20 \AA range. Due to the limited sample size of WLQs, we cannot observe any statistically significant changes at C IV REW $< 10 \text{ \AA}$, which also prevents statistically significant differentiation of the extreme and bridge subsample areas in Figure 7(b).

Although still limited by the sample sizes at low C IV REW, we have now established using a relatively well-defined sample the overall trend that quasars with weaker C IV are more likely to be X-ray weak. This trend is strong, with the X-ray weak fraction declining by a factor of ≈ 13 over the range of C IV REW that we probe. The basic behavior is what is expected from the thick inner-disk model (see Figure 1) put forward by Luo15. Smaller C IV REWs are associated with a thicker inner accretion disk that more effectively blocks ionizing photons from reaching the high-ionization BELR (likely due to higher Eddington ratios in such systems; e.g. Richards et al. 2011; Shen & Ho 2014; Sulentic et al. 2014; Sun et al. 2018). For random quasar orientations on the sky, when the C IV REW is small the thicker inner accretion disk is also more likely to block our line-of-sight to the central X-ray source, leading to a higher fraction of X-ray weakness.

It is challenging to associate the drop in the X-ray weak fraction at C IV REW values of 10–20 \AA with a specific range of the Eddington ratio, but here we provide some basic estimates. For example, if we consider the anti-correlation found between $H\beta$ -based L/L_{Edd} and C IV REW (e.g. Shemmer & Lieber 2015), the inferred L/L_{Edd} is ≈ 1 at 20 \AA and ≈ 4 at 10 \AA . In such a rapid-accretion regime, the inner ac-

cretion flow indeed likely becomes geometrically thick, and this L/L_{Edd} range is consistent with other estimates (see Section 5.3 of Luo15). This being said, the $L/L_{Edd} \approx 1$ –4 range of the L/L_{Edd} vs. C IV REW anti-correlation is not well sampled by observation and is thus uncertain, and $H\beta$ -based estimates of black-hole masses may become unreliable for such rapidly accreting systems (e.g. Marconi et al. 2009). Thus, the estimated L/L_{Edd} values associated with the drop in X-ray weak fraction should be considered with caution.

Considering the model in Figure 1, the lack of clear dependence of the X-ray weak fraction upon C IV REW for C IV REW values of ≈ 4 –10 \AA is somewhat surprising. Based on this range in C IV REW of a factor of ≈ 2.5 , in a shielding model one might have expected a rise by a similar factor in the X-ray weak fraction toward small C IV REW values. However, we do not consider this discrepancy highly problematic at present given the small sample sizes and the fact that other factors will also influence C IV REW values (e.g. gas metallicity and anisotropic line emission; see Section 1.1). Further observations are required for proper assessment of this issue.

5.3 Spectral tracers of X-ray weakness

Previous studies (e.g. Gibson et al. 2008; Luo et al. 2015) have demonstrated that various UV emission-line and continuum properties may be tracers of X-ray weakness among quasars. Nonparametric correlation tests are an effective probe of potential links between UV properties and $\Delta\alpha_{OX}$. The Spearman rank-order test in the Astronomical Survival Analysis package (ASURV; e.g. Feigelson & Nelson 1985; Lavalley et al. 1992) was performed to check whether such correlations exist for several UV emission-line/continuum properties including the REW, blueshift, and FWHM of

C IV; REWs of the Si IV, $\lambda 1900$, Fe II, Fe III, and Mg II emission features; and the relative SDSS color $\Delta(g-i)$. We have also applied the Peto-Prentice test (Prentice & Marek 1979) in the ASURV package (e.g. Feigelson & Nelson 1985; Lavalley et al. 1992) to assess whether X-ray weak WLQs differ from X-ray normal WLQs in their UV properties. The results are presented in Table 7. All the above statistical tests were done for both the representative sample and the full sample. In addition, we have verified that the inclusion of sources with radio detections does not affect the results significantly.

5.3.1 Relative SDSS color $\Delta(g-i)$

The SDSS color $g-i$ has a redshift dependence (e.g. Richards et al. 2001), since the corresponding rest-frame wavelength ranges of the g band and i band change with redshift. Typical rest-frame wavelengths being covered in our study (with a median redshift of $z \approx 1.9$) by the g band and i band are $1300-1900 \text{ \AA}$ and $2300-2900 \text{ \AA}$, respectively. In order to require the relative SDSS color $\Delta(g-i)$ ⁴ to reflect UV (rather than optical) properties, we only utilize WLQs with $z > 1$ when carrying out statistical tests of $\Delta(g-i)$ in the case of the full sample.

While Gallagher et al. (2005) found no correlation between $\Delta(g-i)$ and $\Delta\alpha_{\text{OX}}$ with a quasar sample of either large or small C IV blueshifts, Luo15 found the correlation to be significant among WLQs that typically have large C IV blueshifts as well as small C IV REWs. As can be seen from Figure 8, the null probability that there is no correlation between $\Delta(g-i)$ and $\Delta\alpha_{\text{OX}}$ is small.⁵ In the Peto-Prentice test table (Table 7), the relative color $\Delta(g-i)$ is found to be the most-powerful UV tracer: X-ray weak WLQs have redder $\Delta(g-i)$ than X-ray normal WLQs at nearly the 4σ significance level (3.9σ) in the full sample. Since there is no censoring for $\Delta(g-i)$, the Peto-Prentice test reduces to Gehan's Wilcoxon test (e.g. Lavalley et al. 1992). In the representative sample, the median $\Delta(g-i)$ color among X-ray weak WLQs is 0.10 ± 0.04 (the 1σ uncertainty is derived from bootstrap resampling), and it is 0.00 ± 0.03 among X-ray normal WLQs. In the full sample, $\Delta(g-i)$ is 0.11 ± 0.02 for X-ray weak WLQs, and 0.00 ± 0.03 for X-ray normal WLQs. The distributions of $\Delta(g-i)$ among X-ray weak and X-ray normal WLQs in both the representative sample and the full sample are presented in Figure 9 with the results from the Anderson-Darling test (A-D test; Anderson & Darling 1952; applicable when there is no censoring) in the SciPy package (Jones et al. 2001) listed, also showing the clear distinction. Thus, the relative color $\Delta(g-i)$ appears to be an effective UV tracer of X-ray weakness. As mentioned in Section 1.2, this is plausibly consistent with the thick inner-disk model.

⁴ $\Delta(g-i) = (g-i) - \langle (g-i) \rangle_{\text{redshift}}$, where $\langle (g-i) \rangle_{\text{redshift}}$ is the median $g-i$ color of SDSS quasars at a given redshift (see Richards et al. 2003 for details).

⁵ The correlation becomes even more significant if the radio-detected objects are dropped. For the representative sample, the P_{null} of the Spearman rank-order test turns out to be 0.02; for the full sample, the P_{null} turns out to be 2×10^{-4} .

5.3.2 Fe II REW

Fe II REW was raised as another spectral diagnostic of X-ray weak WLQs together with $\Delta(g-i)$ in Luo15. The correlation between Fe II REW and $\Delta\alpha_{\text{OX}}$ is significant in the full sample, but not significant in the representative sample (see Figure 10 with the Spearman rank-order test results listed). One possibility for the significant correlation in the full sample is that it is artificial and simply driven by complex selection effects associated with the full sample (in Luo15, nearly half of the WLQs studied were originally selected and targeted with additional requirements for strong Fe II emission). Alternatively, the correlation found in the full sample may be real but simply not detectable in the representative sample owing to its smaller size. By randomly sampling 32 (the number of WLQs in the representative sample) objects from WLQs in the full sample, we estimated that the probability of getting significant Spearman rank-order test results ($P < 0.05$) given the current sample size is $\approx 69.8\%$, derived from the empirical distribution of simulated test statistics. Thus, the small sample size could limit our ability of assessing Fe II REW as an effective UV tracer of X-ray weakness among WLQs.

The results from the Peto-Prentice test (see Figure 11 and Table 7) also show that the difference in Fe II REW distributions between X-ray normal WLQs and X-ray weak WLQs is significant in the full sample but not significant in the representative sample. By randomly sampling 14 (the number of X-ray weak WLQs in the representative sample) objects from all the X-ray weak WLQs in the full sample and 18 (the number of X-ray normal WLQs in the representative sample) objects from all the X-ray normal WLQs in the full sample, we estimated that the probability of getting significant Peto-Prentice test results ($P < 0.05$) given the current sample size is $\approx 61.1\%$. Clearly, only a larger unbiased WLQ sample with more detected X-ray weak objects could help us investigate the potential of Fe II REW as a UV tracer of X-ray weakness.

5.3.3 Other emission features

For the remaining spectral properties, including C IV blueshift; C IV FWHM; C IV REW; and REWs of the Si IV, $\lambda 1900$, Fe III, and Mg II emission features, the Peto-Prentice test results in Table 7 reveal that the differences of property distributions between X-ray weak WLQs and X-ray normal WLQs can be found at the $0.08-0.9\sigma$ level for the representative sample and the $0.03-1.4\sigma$ level for the full sample. Thus, they are not effective UV tracers of X-ray weakness. Leaving aside the ambiguous tracer Fe II REW, all the tested emission-line properties fail to distinguish significantly between X-ray weak WLQs and X-ray normal WLQs. In the context of Figure 1, the lack of a connection between C IV FWHM and X-ray weakness is perhaps not surprising, since Runnoe et al. (2013) have shown that C IV FWHM is not a reliable orientation indicator.

5.3.4 Assessments over a broader range of C IV REW and blueshift

Although C IV REW has worked effectively as the primary selector of our WLQs, it does not trace X-ray weakness by

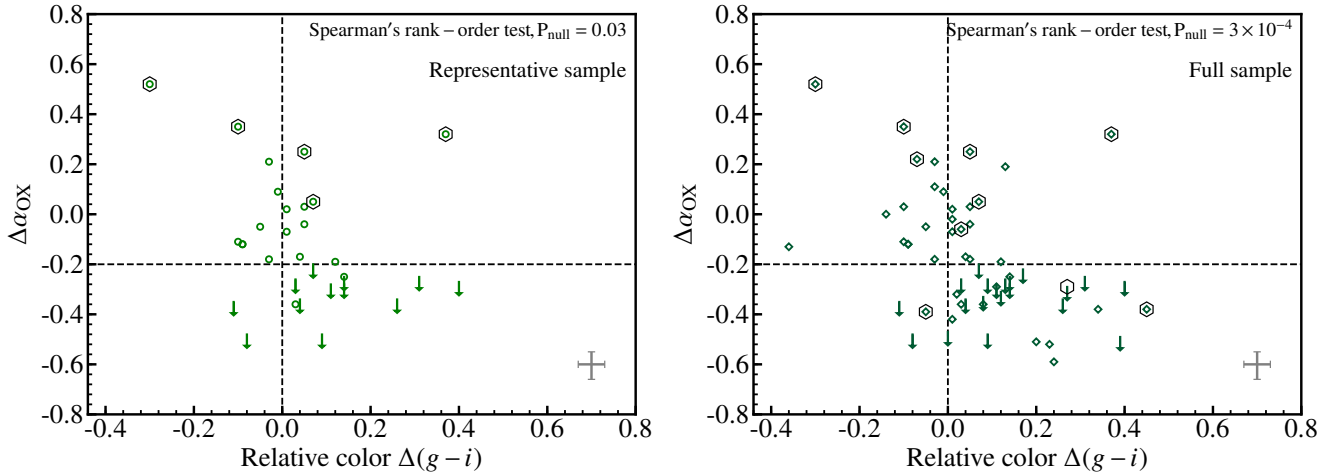


Figure 8. $\Delta\alpha_{\text{OX}}$ vs. relative color for the representative sample (left) and the full sample (right). In cases of X-ray non-detections, the 90% confidence upper limits of $\Delta\alpha_{\text{OX}}$ are represented by the downward arrows. The black hexagons encircling some of the WLQs indicate radio detections of these objects. The median uncertainties of $\Delta\alpha_{\text{OX}}$ and $\Delta(g-i)$ are shown as gray error bars in the bottom-right corners of both panels, and account only for the dominant error factors; i.e., the measurement errors of $\Delta\alpha_{\text{OX}}$ and magnitudes. The horizontal dashed lines display the division between X-ray normal and X-ray weak quasars adopted in this study. The vertical dashed lines display the median color of SDSS quasars. The test results from the Spearman rank-order test are listed for both panels, suggesting the correlation between $\Delta(g-i)$ and $\Delta\alpha_{\text{OX}}$.

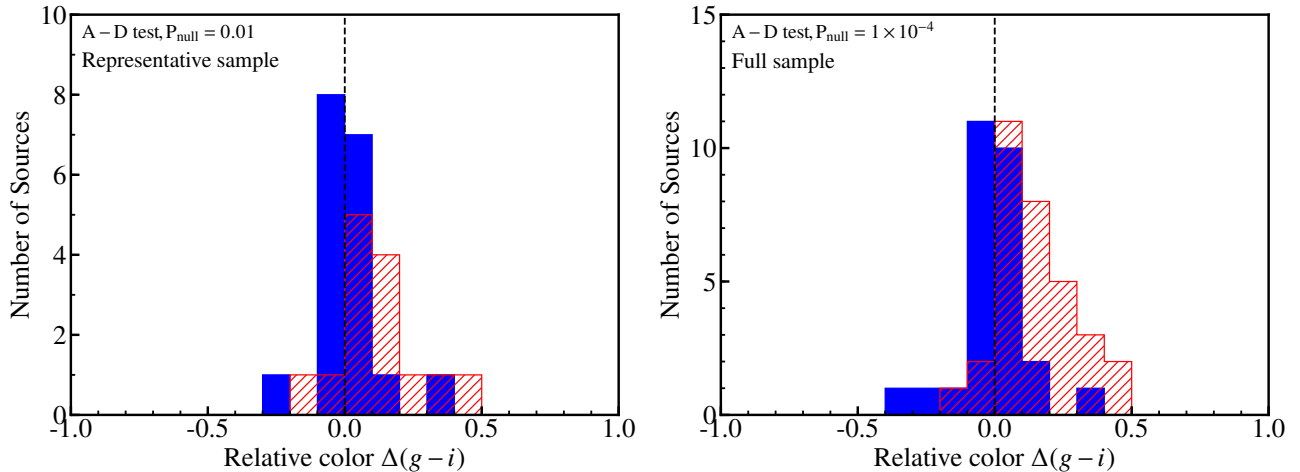


Figure 9. Distributions of the relative color, $\Delta(g-i)$, for the representative sample (left) and the full sample (right). The hatched red histograms represent X-ray weak quasars, while the solid blue histograms are the X-ray normal quasars. The vertical dashed line in each panel indicates a $\Delta(g-i)$ of zero. The probabilities from the A-D test assessing whether the two distributions are drawn from the same population are displayed in both panels, suggesting the difference between the $\Delta(g-i)$ distributions of X-ray weak WLQs and X-ray normal WLQs for both the representative sample and the full sample. In general, X-ray weak WLQs are redder than X-ray normal WLQs (and typical SDSS quasars).

itself particularly well among WLQs. For quasars with larger values of C IV REW (primarily 15–100 Å), however, Gibson et al. (2008) show that $\Delta\alpha_{\text{OX}}$ is correlated with C IV REW at $> 99.9\%$ confidence. Furthermore, for such quasars, Gibson et al. (2008) find that $\Delta\alpha_{\text{OX}}$ is correlated with the measured C IV blueward wavelength shift at 97–99% confidence. It is therefore of interest to consider connections between $\Delta\alpha_{\text{OX}}$ and C IV properties more broadly when our WLQ sample is combined with the Gibson et al. (2008) sample.

Figure 12 shows $\Delta\alpha_{\text{OX}}$ vs. C IV REW and C IV blueshift. The relation between $\Delta\alpha_{\text{OX}}$ and C IV REW is apparent for C IV REWs of 15–100 Å, although even in this range the re-

lation has considerable scatter and thus the slope of the relation is poorly constrained. At lower values of C IV REW, below ≈ 15 Å, the scatter of $\Delta\alpha_{\text{OX}}$ abruptly becomes very large, so that one can no longer identify a clear relation between $\Delta\alpha_{\text{OX}}$ and C IV REW (and, indeed, the Spearman rank-order test finds no significant correlation in this regime). Some WLQs do not appear to be X-ray weak and may even be X-ray stronger than expected from an extrapolation of the $\Delta\alpha_{\text{OX}}$ vs. C IV REW relation to small values of C IV REW. On the other hand, stacking analyses show that many of the WLQs lie far below the extrapolation of the $\Delta\alpha_{\text{OX}}$ vs. C IV REW relation (see the black stars in Figure 12). In

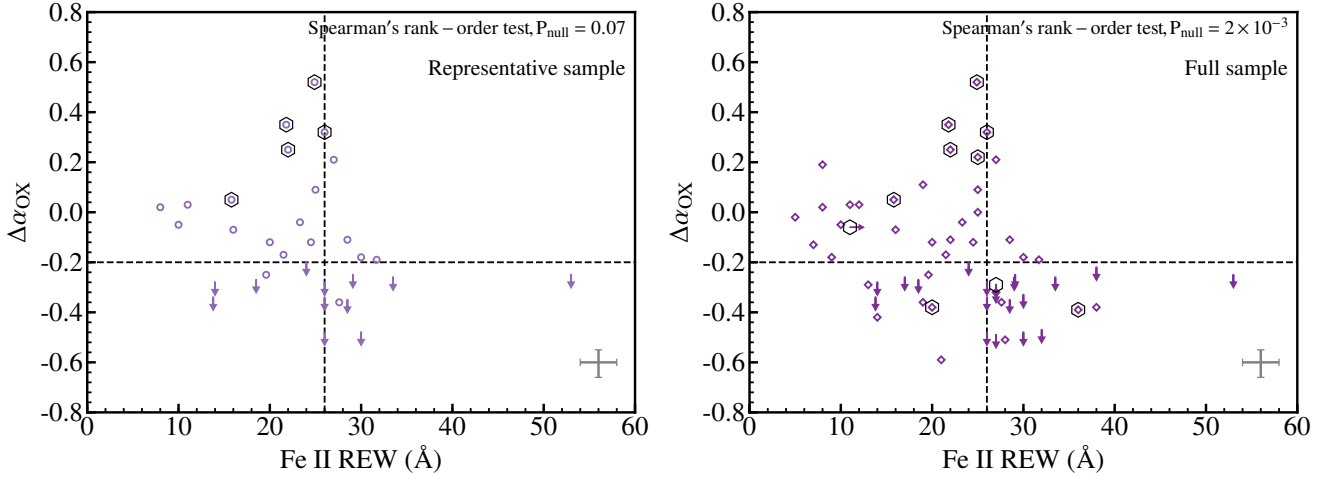


Figure 10. $\Delta\alpha_{\text{OX}}$ vs. Fe II REW for the representative sample (left) and the full sample (right). In cases of X-ray non-detections, the 90% confidence upper limits of $\Delta\alpha_{\text{OX}}$ are represented by the downward arrows. The black hexagons encircling some of the WLQs indicate radio detections of these objects. The object in the full sample that only has limited spectral coverage of Fe II (see the note of Table 3 in Luo15) is represented by the rightward arrow in the right panel. The median uncertainties of $\Delta\alpha_{\text{OX}}$ and Fe II REW are shown as gray error bars in the bottom-right corners of both panels, and account only for the dominant error factors; i.e., the measurement errors. The horizontal dashed lines display the division between X-ray normal and X-ray weak quasars adopted in this study. The vertical dashed lines indicate the Fe II REW of the composite SDSS spectrum from Vanden Berk et al. (2001). The test results from the Spearman rank-order test are listed for both panels, suggesting that while the correlation between Fe II REW and $\Delta\alpha_{\text{OX}}$ is significant in the full sample, it is not significant in the representative sample.

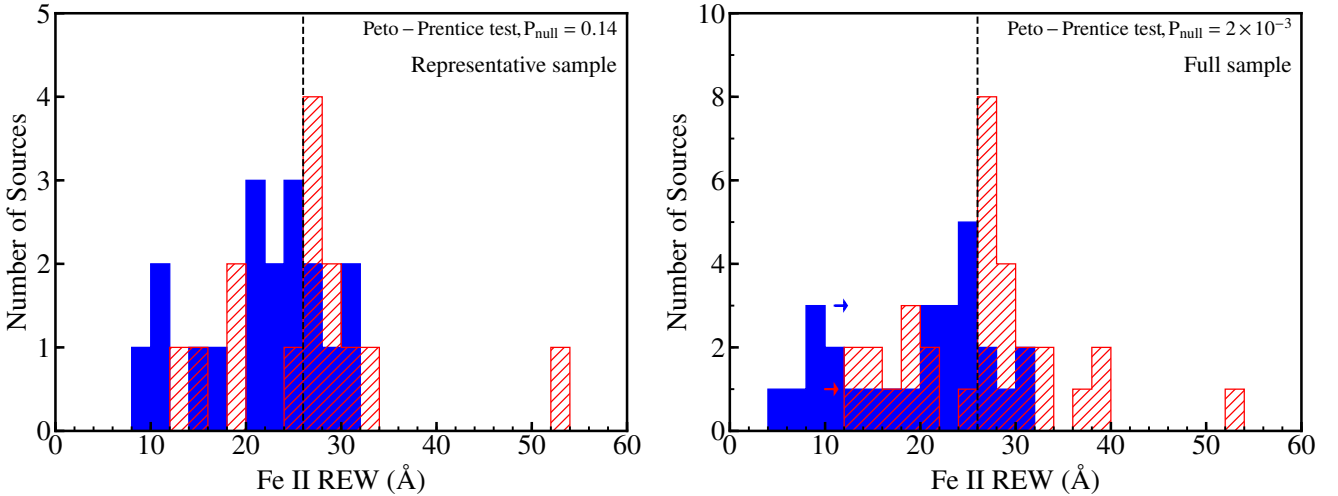


Figure 11. Distributions of the Fe II REWs for the representative sample (left) and the full sample (right). The hatched red histograms represent X-ray weak quasars, while the solid blue histograms are X-ray normal quasars. The red/blue arrows represent limits of Fe II REWs measured from X-ray weak/X-ray normal quasars (see the note of Table 3, Luo15). The vertical dashed lines indicate the Fe II REW of the composite SDSS spectrum from Vanden Berk et al. (2001). The probabilities from the Peto-Prentice test are displayed in both panels, indicating that while the difference between the Fe II REW distributions of X-ray weak WLQs and X-ray normal WLQs is significant in the full sample, it is not significant in the representative sample.

the context of the shielding model shown in Figure 1, this $\Delta\alpha_{\text{OX}}$ diversity, corresponding to a range of > 100 in relative X-ray vs. optical/UV flux, is largely attributable to high-inclination objects being obscured by the thick inner disk while low-inclination objects are not. However, the fact that some WLQs appear X-ray strong relative to the extrapolated $\Delta\alpha_{\text{OX}}$ vs. C IV REW relation is puzzling. Several factors may be relevant to explaining this result. First, as noted above, the relation established at C IV REW of 15–100 Å has sig-

nificant uncertainty in its slope, and thus its extrapolation below 15 Å is uncertain on basic statistical grounds. Furthermore, it is not entirely clear that the relation can be appropriately extrapolated outside the domain where it was derived by a factor of 2–15 times in C IV REW. Finally, we note that most of the strongest outliers toward positive $\Delta\alpha_{\text{OX}}$ are radio-detected objects that may have some jet-linked contribution to their X-ray fluxes (see Section 4.5 for further discussion). A large-scale study of the $\Delta\alpha_{\text{OX}}$ vs. C IV

REW relation utilizing archival data would be valuable for clarifying these issues.

The plot of $\Delta\alpha_{\text{OX}}$ vs. C IV blueshift in Figure 12 does not show any tight correlation over blueshifts ranging from -6000 km s^{-1} to $+1000 \text{ km s}^{-1}$. The scatter in $\Delta\alpha_{\text{OX}}$ at a given C IV blueshift for WLQs is clearly large. The uncertainty of the slope of the $\Delta\alpha_{\text{OX}}$ vs. C IV blueshift relation for the Gibson et al. (2008) quasars is large, making extrapolation to the large blueshifts of WLQs highly uncertain.

6 SUMMARY AND FUTURE WORK

6.1 Summary of main results

We have presented X-ray and multiwavelength analyses of 32 WLQs that have been selected in an unbiased and consistent manner, thereby bridging the observational gap between WLQs and typical quasars and connecting their X-ray properties. The main points from this paper are the following:

(i) We selected 20 representative WLQs with C IV REW $\approx 5 - 15 \text{ \AA}$ and obtained *Chandra* observations of 14 of these having no sensitive archival X-ray observations. X-ray photometric analyses and UV emission-line measurements were performed for the 20 objects. After combining this dataset with another 12 representative WLQs that have C IV REW $< 5 \text{ \AA}$, we re-divided these 32 WLQs into two subsamples (extreme/bridge) based on their C IV REW with equal numbers of objects (16/16 with C IV REW below/above 7 \AA) to probe the relationships of UV and X-ray properties. See Sections 2, 3, and 4.3.

(ii) We calculated $\Delta\alpha_{\text{OX}}$ for our *Chandra* Cycle 17 sample objects and the archival objects that had not been previously analyzed. We also performed X-ray stacking analyses to derive the average properties of our X-ray weak WLQs since their limited numbers of detected counts prevented us from analyzing them individually. All the WLQs in the representative sample have IR-to-UV SEDs similar to those of typical quasars, indicating that $\Delta\alpha_{\text{OX}}$ can be appropriately used to assess the level of line-of-sight X-ray emission relative to the longer wavelength SED. The representative WLQs are also radio-quiet ($R < 10$), minimizing the influence from jets on the observed X-ray properties. See Sections 4.1, 4.2, 4.4, and 4.5.

(iii) The hard power-law (0.5–8 keV, corresponding to $\approx 2\text{--}23 \text{ keV}$ in the rest frame) effective photon index, $\Gamma_{\text{eff}} = 1.19^{+0.56}_{-0.45}$, measured from X-ray stacking of 14 X-ray weak WLQs in the representative sample, suggests that the observed X-ray weakness may be generally explained by heavy absorption due to small-scale shielding. This is consistent with the thick inner-disk model. See Section 5.1.

(iv) A total of 7 out of 16 ($43.8^{+12.4}_{-11.0}\%$) WLQs in the bridge subsample are X-ray weak, and this also applies to the extreme subsample. Comparing with typical quasars in Gibson et al. (2008) Sample B, we established and quantified an overall trend, that is especially pronounced in the 10–20 \AA range, demonstrating that quasars with weaker C IV REW are more likely to be X-ray weak. This trend is strong; the fraction of X-ray weak quasars varies by a factor of ≈ 13 for C IV REW ranging from 4–50 \AA . The trend is expected from the shielding model, and thus these results generally support

the model. As the inner accretion disk becomes thicker, ionizing radiation is increasingly blocked from reaching the C IV BELR and, for random orientations, our line of sight to the central X-ray emitting region is more likely to be blocked. See Section 5.2.

(v) Among the UV continuum and emission-line properties examined that might be tracers of X-ray weakness among WLQs, the relative SDSS color $\Delta(g-i)$ proved to be the most effective tracer. X-ray weak WLQs have redder $\Delta(g-i)$ (at 3.9σ significance). See Section 5.3.

6.2 Future work

There are a number of ways the results in this paper might be extended. For example, the current sizes of our extreme and bridge WLQ subsamples remain small, and these should be enlarged via additional X-ray observations for improved power in statistical hypothesis testing and trend quantification. Such improved samples (selected with a lower m_i threshold) would allow better quantification of how the fraction of X-ray weak quasars depends upon C IV REW with implications for the thick inner-disk model; see Figure 7(a). Note that the observed dependence is particularly strong for C IV REW = 10–20 \AA , thus, increasing the sample size in this C IV REW range may be particularly useful. In addition to increasing the sizes of the extreme and bridge subsamples, improving the data quality for their constituent objects is also important. Presently, many of the objects in these samples are X-ray undetected, so that only limits on their $\Delta\alpha_{\text{OX}}$ values are available (and these $\Delta\alpha_{\text{OX}}$ limits are often relatively loose). While we have been able to recover useful information from these undetected objects via survival analysis and stacking, reducing the fraction of X-ray upper limits would provide a clearer picture of the overall population. For example, we would be able to examine the distribution of $\Delta\alpha_{\text{OX}}$ values, assessing potential diversity within the WLQ population (e.g. the possible presence of some intrinsically X-ray weak objects), and our X-ray spectral analyses would also benefit from the additional detected counts. We would furthermore be able to investigate the general UV spectral tracers of X-ray weakness more effectively via correlation analyses. Considering our stacking results, we should be able to detect most of the currently X-ray undetected sources with exposure times $\approx 5 - 10$ times longer than the present ones. While such exposures would not be inexpensive, they are not impracticable.

Furthermore, in the construction of our WLQ samples, we deliberately excluded quasars with significant C IV absorption (e.g. BALs and mini-BALs) and also those with very red UV spectra (see Section 2.1). While this was necessary and appropriate for this project, it would now be useful to target such objects with *Chandra* and *XMM-Newton* so that their X-ray properties could be connected with those of the WLQs in our current samples. This seems especially relevant given that we find a connection between X-ray weakness and red UV color (Section 5.3) and given that the fraction of quasars with BALs likely rises with Eddington ratio (e.g. Boroson 2002; Ganguly et al. 2007). Ideally, one would like to study the fraction of X-ray weak quasars vs. C IV REW relation (Figure 7(a)) with such objects included, though this will likely be technically challenging (e.g. measurements

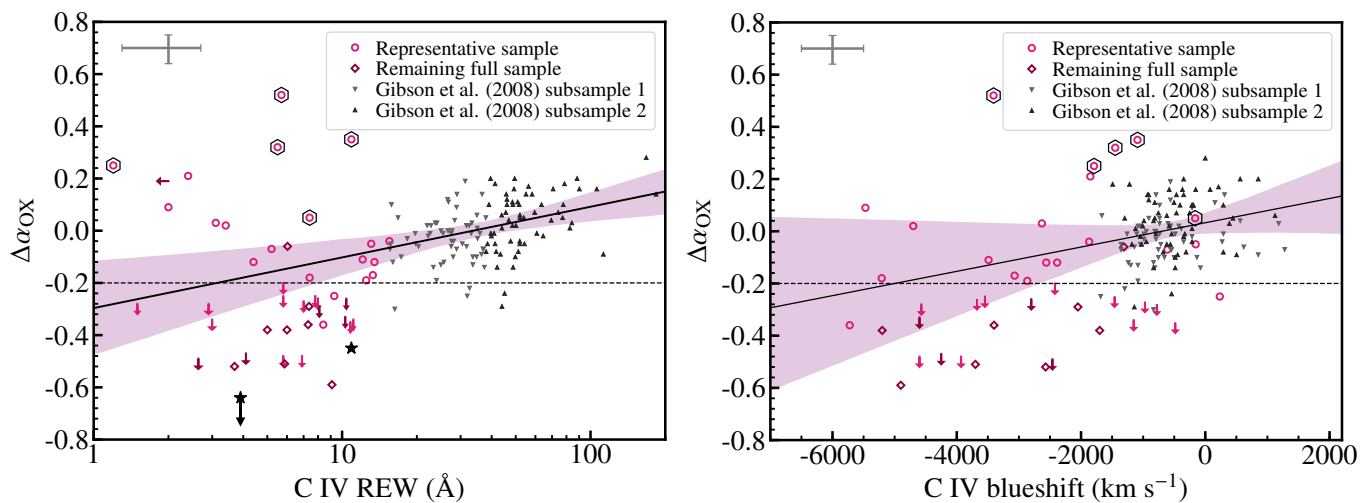


Figure 12. $\Delta\alpha_{\text{OX}}$ vs. C IV REW (left) and $\Delta\alpha_{\text{OX}}$ vs. C IV blueshift (right). The representative sample, the remaining part of the full sample (which consists of WLQs that are not included in the representative sample), and two subsamples of the Gibson et al. (2008) Sample B quasars are distinguished using symbol types as labeled. In cases of X-ray non-detections, the 90% confidence upper limits of $\Delta\alpha_{\text{OX}}$ are represented by the downward arrows. The leftward arrow in the left panel presents the 3σ upper limit of C IV REW. The black hexagons encircling some of the WLQs indicate radio detections of these objects. In the left/right panel, the median measurement errors of $\Delta\alpha_{\text{OX}}$ and C IV REW/C IV blueshift for WLQs are shown as gray error bars in the upper-left corner. The two black stars in the $\Delta\alpha_{\text{OX}}$ vs. C IV REW (left) panel represent the X-ray stacking results: the one with an arrow represents the 90% confidence upper limit of $\Delta\alpha_{\text{OX}}$ derived from the X-ray weak WLQs in the extreme subsample, and the one without an arrow represents the stacked mean $\Delta\alpha_{\text{OX}}$ of X-ray weak WLQs in the bridge subsample, each plotted at the median C IV REW of WLQs in the subsample. In both panels, the black solid line represents the posterior median estimate of the regression line obtained through fitting our “ultra-clean” version of the Gibson et al. (2008) Sample B quasars following the method in Kelly (2007), and the shaded region represents the 3σ pointwise confidence intervals on the regression line. The horizontal dashed lines indicate the division between X-ray normal and X-ray weak quasars adopted in this study.

of the C IV REW may be affected by C IV absorption and complex intrinsic reddening).

In addition, several of the main results in this work have been derived by comparing our WLQ subsamples with the archival X-ray quasar sample of Gibson et al. (2008) (specifically, their Sample B). In the decade since Sample B was created, both the X-ray archives and underlying SDSS quasar database have grown substantially. Further data mining based on the current X-ray archives and SDSS database could define a substantially larger version of this sample for more statistically powerful comparisons with WLQs.

Finally, we note that our thick inner-disk model for WLQs has similarities with models of other rapidly accreting systems, including stellar tidal disruption events (TDEs; e.g. Dai et al. 2018) and ultraluminous X-ray sources (ULXs; e.g. Kaaret et al. 2017). For example, Dai et al. (2018) suggest that the X-ray vs. optical fluxes of TDEs will have an inclination-angle dependence that is qualitatively similar to what we previously proposed for WLQs, due to obscuration of small-scale X-ray emission by a thick accretion disk and its associated outflow. Along these lines, one might speculate that WLQs have a (slow) transient nature as well. Their SMBHs are likely too massive typically to allow tidal disruptions of stars (e.g. see Section 5.3 of Luo15 for SMBH mass estimates), but captures of 10^3 – $10^6 M_{\odot}$ nuclear molecular clouds are plausible and could feed the SMBH at a super-Eddington rate for decades to millennia. Generally, comparisons of the properties of WLQs, TDEs, and ULXs should be productive for interpreting the nature of all three classes and suggesting valuable new observations.

ACKNOWLEDGEMENTS

We thank Fabio Vito and Shifu Zhu for helpful discussions. QN and WNB acknowledge support from Chandra X-ray Center grant GO6-17083X, the NASA ADP Program, and the Penn State ACIS Instrument Team Contract SV4-74018 (issued by the Chandra X-ray Center, which is operated by the Smithsonian Astrophysical Observatory for and on behalf of NASA under contract NAS8-03060). The Guaranteed Time Observations (GTO) for some of the quasars studied were selected by the ACIS Instrument Principal Investigator, Gordon P. Garmire, currently of the Huntingdon Institute for X-ray Astronomy, LLC, which is under contract to the Smithsonian Astrophysical Observatory; Contract SV2-82024. BL acknowledges financial support from the National Key R&D Program of China grant 2016YFA0400702 and the National Natural Science Foundation of China grant 11673010. PBH acknowledges support from NSERC, funding reference number 2017-05983. YS acknowledges support from an Alfred P. Sloan Research Fellowship and NSF grant AST-1715579. RMP acknowledges support from Curtin University through the Peter Curran Memorial Fellowship.

REFERENCES

- Abramowicz M. A., et al., 1988, *ApJ*, **332**, 646
- Anderson T. W., Darling D. A., 1952, *The annals of mathematical statistics*, pp 193–212
- Bañados E., et al., 2016, *ApJS*, **227**, 11
- Becker R. H., White R. L., Helfand D. J., 1995, *ApJ*, **450**, 559

- Boller T., et al., 2016, *A&A*, **588**, A103
- Boroson T. A., 2002, *ApJ*, **565**, 78
- Brightman M., et al., 2013, *MNRAS*, **433**, 2485
- Broos P. S., et al., 2007, *ApJS*, **169**, 353
- Cameron E., 2011, *Publ. Astron. Soc. Australia*, **28**, 128
- Cardelli J. A., Clayton G. C., Mathis J. S., 1989, *ApJ*, **345**, 245
- Cohen M., Wheaton W. A., Megeath S. T., 2003, *AJ*, **126**, 1090
- Dai L., et al., 2018, preprint, ([arXiv:1803.03265](https://arxiv.org/abs/1803.03265))
- Diamond-Stanic A. M., et al., 2009, *ApJ*, **699**, 782
- Dickey J. M., Lockman F. J., 1990, *ARA&A*, **28**, 215
- Elvis M., 2012, in Chartas G., Hamann F., Leighly K., eds, ASP Conf. Ser. Vol. 460, AGN Winds in Charleston. p. 186
- Fan X., et al., 1999, *ApJ*, **526**, L57
- Feigelson E. D., Nelson P. I., 1985, *ApJ*, **293**, 192
- Fruscione A., et al., 2006, in Society of Photo-Optical Instrumentation Engineers (SPIE) Conference Series. p. 62701V, [doi:10.1117/12.671760](https://doi.org/10.1117/12.671760)
- Gallagher S. C., et al., 2005, *AJ*, **129**, 567
- Ganguly R., et al., 2007, *ApJ*, **665**, 990
- Garmire G. P., et al., 2003, in Truemper J. E., Tananbaum H. D., eds, Proc. SPIE. Vol. 4851, X-Ray and Gamma-Ray Telescopes and Instruments for Astronomy.. pp 28–44, [doi:10.1117/12.461599](https://doi.org/10.1117/12.461599)
- Gehrels N., 1986, *ApJ*, **303**, 336
- Gibson R. R., Brandt W. N., Schneider D. P., 2008, *ApJ*, **685**
- Hewett P. C., Wild V., 2010, *MNRAS*, **405**, 2302
- Hryniewicz K., et al., 2010, *MNRAS*, **404**, 2028
- Jiang Y.-F., Stone J. M., Davis S. W., 2014, *ApJ*, **796**
- Jiang Y.-F., Stone J., Davis S. W., 2018, preprint, ([arXiv:1709.02845](https://arxiv.org/abs/1709.02845))
- Jones E., Oliphant T., Peterson P., et al., 2001, SciPy: Open source scientific tools for Python, <http://www.scipy.org/>
- Just D. W., et al., 2007, *ApJ*, **665**, 1004
- Kaaret P., Feng H., Roberts T. P., 2017, *ARA&A*, **55**, 303
- Kellermann K. I., et al., 1989, *AJ*, **98**, 1195
- Kelly B. C., 2007, *ApJ*, **665**, 1489
- Knuth K. H., 2006, preprint, ([arXiv:physics/0605197](https://arxiv.org/abs/physics/0605197))
- Kraft R. P., Burrows D. N., Nousek J. A., 1991, *ApJ*, **374**, 344
- Lane R. A., et al., 2011, *ApJ*, **743**
- Laor A., Davis S. W., 2011, *MNRAS*, **417**, 681
- Lavalley M., Isobe T., Feigelson E., 1992, in Worrall D. M., Biemesderfer C., Barnes J., eds, ASP Conf. Ser. Vol. 25, Astronomical Data Analysis Software and Systems I. p. 245
- Leighly K. M., 2004, *ApJ*, **611**, 125
- Leighly K. M., et al., 2007, *ApJ*, **663**, 103
- Luo B., et al., 2013, *ApJ*, **772**
- Luo B., et al., 2015, *ApJ*, **805**
- Lusso E., et al., 2010, *A&A*, **512**
- Lyons L., 1991, A Practical Guide to Data Analysis for Physical Science Students. Cambridge Univ. Press
- Marconi A., et al., 2009, *ApJ*, **698**, L103
- Martin D. C., et al., 2005, *ApJ*, **619**, L1
- Miller B. P., et al., 2011, *ApJ*, **726**
- O'Donnell J. E., 1994, *ApJ*, **422**, 158
- Park T., et al., 2006, *ApJ*, **652**, 610
- Planck Collaboration et al., 2016, *A&A*, **594**
- Plotkin R. M., et al., 2010, *AJ*, **139**, 390
- Plotkin R. M., et al., 2015, *ApJ*, **805**
- Prentice R. L., Marek P., 1979, *Biometrics*, pp 861–867
- Reeves J. N., et al., 1997, *MNRAS*, **292**, 468
- Richards G. T., et al., 2001, *AJ*, **121**, 2308
- Richards G. T., et al., 2003, *AJ*, **126**, 1131
- Richards G. T., et al., 2006, *ApJS*, **166**, 470
- Richards G. T., et al., 2011, *AJ*, **141**
- Richstone D. O., Schmidt M., 1980, *ApJ*, **235**, 361
- Risaliti G., Young M., Elvis M., 2009, *ApJ*, **700**, L6
- Runnoe J. C., et al., 2013, *MNRAS*, **429**, 135
- Saxton R. D., et al., 2008, *A&A*, **480**, 611
- Schneider D. P., et al., 2010, *AJ*, **139**, 2360
- Scott A. E., et al., 2011, *MNRAS*, **417**, 992
- Shemmer O., Lieber S., 2015, *ApJ*, **805**
- Shemmer O., et al., 2008, *ApJ*, **682**
- Shemmer O., et al., 2010, *ApJ*, **722**, L152
- Shen Y., Ho L. C., 2014, *Nature*, **513**, 210
- Shen Y., Kelly B. C., 2012, *ApJ*, **746**, 169
- Shen Y., et al., 2011, *ApJS*, **194**
- Sądowski A., 2009, *ApJS*, **183**, 171
- Sądowski A., 2011, preprint, ([arXiv:1108.0396](https://arxiv.org/abs/1108.0396))
- Sądowski A., et al., 2014, *MNRAS*, **439**, 503
- Sądowski A., et al., 2015, *MNRAS*, **447**, 49
- Skrutskie M. F., et al., 2006, *AJ*, **131**, 1163
- Steffen A. T., et al., 2006, *AJ*, **131**, 2826
- Strateva I. V., et al., 2005, *AJ*, **130**, 387
- Sulentic J. W., et al., 2014, *A&A*, **570**
- Sun M., et al., 2018, *ApJ*, **854**
- Vanden Berk D. E., et al., 2001, *AJ*, **122**, 549
- Vignali C., Brandt W. N., Schneider D. P., 2003, *AJ*, **125**, 433
- Wang J.-M., et al., 2014, *ApJ*, **797**
- White R. L., et al., 1997, *ApJ*, **475**, 479
- Wilkes B. J., et al., 1994, *ApJS*, **92**, 53
- Wright E. L., et al., 2010, *AJ*, **140**
- Wu J., et al., 2011, *ApJ*, **736**
- Wu J., et al., 2012, *ApJ*, **747**
- Xue Y. Q., et al., 2011, *ApJS*, **195**
- York D. G., et al., 2000, *AJ*, **120**, 1579

Table 1. Summary of Utilized Quasar Samples

Sample Name	Number of Sources	Range of C IV REW (Å)	Median C IV REW (Å)	Range of Redshift	Median Redshift	Range of $\log L_{2500 \text{ Å}}$ ($\text{erg s}^{-1} \text{ Hz}^{-1}$)	Median $\log L_{2500 \text{ Å}}$ ($\text{erg s}^{-1} \text{ Hz}^{-1}$)	Relevant Section	Notes
(1)	(2)	(3)	(4)	(5)	(6)	(7)	(8)	(9)	(10)
Extreme Subsample ^a	16	0–7.0	3.9 ± 0.9	1.5–2.5	1.83 ± 0.08	30.95–31.75	31.28 ± 0.06	2.2	WLQ
Bridge Subsample	16	7.0–15.5	10.9 ± 1.2	1.7–2.2	1.92 ± 0.06	31.15–31.89	31.40 ± 0.06	2.2	WLQ
Representative Sample ^b	32	0–15.5	7.0 ± 0.9	1.5–2.5	1.87 ± 0.06	30.95–31.89	31.35 ± 0.04	2.2	WLQ
Full Sample ^c	63	0–15.5	6.5 ± 0.7	0.4–3.0	1.80 ± 0.05	29.59–32.39	31.26 ± 0.05	2.3	WLQ
Gibson et al. (2008) Subsample 1	59	15.5–38.0	27.7 ± 1.1	1.7–2.7	2.03 ± 0.06	30.33–31.67	31.00 ± 0.06	2.2	Typical quasars
Gibson et al. (2008) Subsample 2	60	38.0–183.6	50.5 ± 1.4	1.7–2.7	1.89 ± 0.03	30.39–31.46	30.86 ± 0.05	2.2	Typical quasars

Note. — Cols. (1) and (2): Sample names utilized in this paper and the number of sources within the sample. Cols. (3) and (4): Range of C IV REW for each sample and median value with the bootstrapped error. Cols. (5) and (6): Range of redshift for each sample and median value with the bootstrapped error. Cols. (7) and (8): Range of logarithm of the monochromatic luminosity at rest-frame 2500 Å for each sample and median value with the bootstrapped error. Col. (9): Relevant sections describing the selection and constitution of each sample. Col. (10): Comments for each sample.

^aMost of the WLQs in the extreme subsample have been well-studied previously and thus are not included in our tables. Detailed multi-wavelength analyses of J082508.75+115536.3, J082722.73+032755.9, J084424.24+124546.5, J100517.54+331202.8, J115637.02+184856.5, J132809.59+545452.7, J134601.28+585820.2, J140710.26+241853.6, J141141.96+140233.9, J141730.92+073320.7, J153913.47+395423.4, and J172858.16+603512.7 can be found in Luo15; detailed multiwavelength analyses of J094533.98+100950.1 and J161245.68+511816.9 can be found in Wu12; detailed multiwavelength analyses of J090312.22+070832.4 can be found in Wu11. Only one object, J113949.39+460012.9 (which has an archival X-ray observation), has not been analyzed before, and it is thus listed in our tables along with WLQs in the bridge subsample.

^bRepresentative sample is the sum of the extreme subsample and bridge subsample.

^cFull sample includes representative sample and other WLQs that are not selected in as systematic a manner. For the full sample, cols (3) and (4) only apply to the 46 objects with SDSS spectral coverage of C IV.

Table 2. X-ray Observations and Photometric Properties of WLQs in the Bridge Subsample

Object Name (J2000) (1)	RA (deg) (2)	Dec (deg) (3)	Redshift (4)	Observation ID (5)	Observation Start Date (6)	Exposure Time (ks) (7)	Soft Band (0.5–2 keV) (8)	Hard Band (2–8 keV) (9)	Band Ratio (10)	Γ_{eff} (11)	Comment (12)
Chandra Cycle 17 Objects											
080040.77 + 391700.4	120.169914	39.283451	1.777	18110	2015 Dec 17	3.1	$8.3^{+4.1}_{-2.9}$	$4.4^{+3.5}_{-2.1}$	$0.52^{+0.50}_{-0.31}$	$1.6^{+0.7}_{-0.5}$...
095023.19 + 024651.7	147.596664	2.781048	1.882	18118	2016 Jan 28	4.8	< 4.0	< 4.2
101209.62 + 324421.4	153.040115	32.739295	1.985	18113	2016 Feb 11	4.2	$7.3^{+3.9}_{-2.7}$	$6.5^{+4.0}_{-2.6}$	$0.89^{+0.73}_{-0.49}$	$1.1^{+0.6}_{-0.4}$...
101945.26 + 211911.0	154.938583	21.319723	1.842	18109	2015 Dec 29	3.1	$11.5^{+4.6}_{-3.4}$	$4.3^{+3.5}_{-2.1}$	$0.38^{+0.34}_{-0.22}$	$1.8^{+0.6}_{-0.5}$...
110409.96 + 434507.0	166.041519	43.751972	1.804	18119	2016 Jan 4	4.6	< 2.4	< 2.5
122048.52 + 044047.6	185.202179	4.679912	1.737	18112	2016 Jan 21	3.4	$7.3^{+3.9}_{-2.7}$	< 4.3	< 0.59	> 1.4	...
122311.28 + 124153.9	185.797028	12.698329	2.068	18115	2016 Feb 11	4.5	< 4.0	< 4.2
122855.90 + 341436.9	187.232941	34.243595	2.147	18111	2016 Feb 15	3.9	< 4.1	< 2.5
124516.46 + 015641.1	191.318604	1.944762	2.006	18114	2016 Feb 22	4.3	$9.3^{+4.3}_{-3.1}$	$12.0^{+4.9}_{-3.6}$	$1.29^{+0.79}_{-0.57}$	$0.9^{+0.4}_{-0.4}$...
140701.59 + 190417.9	211.756653	19.071661	2.004	18117	2016 Apr 5	5.0	$2.0^{+2.8}_{-1.3}$	< 2.5	< 1.42	> 0.8	...
150921.68 + 030452.7	227.340347	3.081327	1.808	18107	2015 Dec 28	3.1	$18.7^{+5.6}_{-4.4}$	$12.1^{+4.9}_{-3.6}$	$0.64^{+0.32}_{-0.24}$	$1.4^{+0.4}_{-0.3}$...
155621.31 + 112433.2	239.088806	11.409227	1.730	18108	2016 May 12	3.1	$7.3^{+3.9}_{-2.7}$	$9.9^{+4.5}_{-3.2}$	$1.36^{+0.97}_{-0.67}$	$0.9^{+0.5}_{-0.4}$...
163810.07 + 115103.9	249.541992	11.851092	1.983	18116	2016 Feb 17	4.1	< 2.4	< 2.5
232519.33 + 011147.8	351.330566	1.196628	1.727	18120	2016 Aug 15	4.3	$7.3^{+3.9}_{-2.7}$	$8.8^{+4.4}_{-3.0}$	$1.21^{+0.89}_{-0.61}$	$1.0^{+0.5}_{-0.4}$...
Archival data											
123326.03 + 451223.0	188.358459	45.206402	1.966	26747	1990 Nov 27	0.5	$21.6^{+6.2a}_{-6.2}$	<i>RASS2RXS</i>
215954.45 – 002150.1	329.976929	-0.363942	1.965	11509	2009 Sep 20	7.9	$106.3^{+11.6}_{-10.5}$	$39.5^{+7.8}_{-6.6}$	$0.37^{+0.08}_{-0.07}$	$1.9^{+0.1}_{-0.2}$	Cycle 11
113949.39 + 460012.9*	174.955795	46.003604	1.859	9155100004	2008 May 29	0.008	$4.0^{+2.0b}_{-2.0}$	<i>XMMSL2</i>

Note. — Col. (1): Object name in the J2000 coordinate format. The object marked with “*” comes from the extreme subsample. Cols. (2)–(3): The SDSS position in decimal degrees. Col. (4): Redshift adopted from [Hewett & Wild \(2010\)](#). Cols. (5)–(6): The ID and start date of *Chandra* observations. Col. (7): Effective exposure time in the full band (0.5–8 keV) with background flares cleaned. Cols. (8)–(9): Source counts (aperture-corrected) in the soft band (0.5–2 keV) and hard band (2–8 keV). If the source is undetected in this band, an upper limit of counts at a 90% confidence level is listed. Col. (10): Ratio of the hard-band and soft-band counts. “...” indicates that the source is not detected in both bands. Col. (11): Effective power-law photon index in the 0.5–8 keV band. “...” indicates that Γ_{eff} cannot be constrained. Col. (12): Comments for the object.

^aFor *RASS2RXS* (Second ROSAT All-Sky Survey Point Source Catalog) data, the soft band is 0.1–2.4 keV.

^bFor *XMMSL2* (Second *XMM-Newton* Slew Survey Catalog) data, the soft band is 0.2–2 keV.

Table 3. X-ray and Optical Properties of Quasars in the Bridge Subsample

Object Name (J2000) (1)	M_i (2)	$N_{\text{H,Gal}}$ (3)	Count Rate (0.5–2 keV) (4)	F_X (0.5–2 keV) (5)	f_2 keV (6)	$\log L_X$ (2–10 keV) (7)	$f_{2500 \text{ \AA}}$ (8)	$\log L_{2500 \text{ \AA}}$ (9)	α_{OX} (10)	$\Delta\alpha_{\text{OX}}(\sigma)$ (11)	f_{weak} (12)	$\Delta(g-i)$ (13)	R (14)
Chandra Cycle 17 Objects													
080040.77+391700.4	−27.93	5.16	$2.70^{+1.34}_{-0.94}$	1.84	6.58	44.77	3.57	31.47	−1.82	−0.12(0.78)	2.01	−0.09	< 1.3
095023.19+024651.7	−27.48	3.66	< 0.85	< 0.52	< 1.75	< 44.32	1.82	31.22	< −1.92	< −0.26(1.59)	> 4.74	0.03	< 2.7
101209.62+324421.4	−27.77	1.78	$1.75^{+0.95}_{-0.65}$	1.06	3.09	44.73	2.42	31.38	−1.88	−0.19(1.23)	3.12	0.12	< 1.8
101945.26+211911.0	−28.08	2.11	$3.73^{+1.50}_{-1.11}$	2.46	9.70	44.89	3.51	31.49	−1.75	−0.05(0.31)	1.32	−0.05	< 1.3
110409.96+434507.0	−27.29	1.21	< 0.53	< 0.31	< 1.02	< 44.05	1.75	31.17	< −2.01	< −0.35(2.11)	> 8.15	0.11	< 2.5
122048.52+044047.6	−27.73	1.65	$2.16^{+1.17}_{-0.80}$	1.44	5.71	44.57	2.69	31.33	−1.79	−0.11(0.72)	1.97	−0.10	< 1.7
122311.28+124153.9	−27.81	2.52	< 0.89	< 0.54	< 1.85	< 44.36	2.05	31.34	< −1.94	< −0.25(1.62)	> 4.57	0.14	< 3.2
122855.90+341436.9	−28.45	1.33	< 1.05	< 0.62	< 2.16	< 44.51	3.29	31.58	< −1.99	< −0.27(1.88)	> 5.15	0.40	< 1.4
124516.46+015641.1	−27.70	1.75	$2.19^{+1.01}_{-0.72}$	1.31	3.40	44.87	2.41	31.39	−1.86	−0.17(1.11)	2.80	0.04	< 1.9
140701.59+190417.9	−27.67	2.41	$0.40^{+0.55}_{-0.27}$	0.26	0.90	44.08	1.78	31.26	−2.03	−0.36(2.24)	8.74	0.03	< 2.6
150921.68+030452.7	−28.40	3.85	$6.10^{+1.81}_{-1.43}$	3.94	13.09	45.16	5.34	31.65	−1.77	−0.04(0.30)	1.29	0.05	< 0.9
155621.31+112433.2	−28.16	3.69	$2.37^{+1.28}_{-0.87}$	1.47	3.86	44.81	5.11	31.60	−1.97	−0.25(1.70)	4.39	0.14	< 0.9
163810.07+115103.9	−27.73	4.56	< 0.59	< 0.37	< 1.25	< 44.21	2.52	31.40	< −2.04	< −0.34(2.24)	> 7.90	0.04	< 1.9
232519.33+011147.8	−27.15	4.40	$1.71^{+0.93}_{-0.63}$	1.11	3.07	44.66	1.82	31.15	−1.83	−0.18(1.05)	2.87	−0.03	< 2.4
Archival data													
123326.03+451223.0	−28.53	1.36	$47.9^{+13.9a}_{-13.9}$	28.81	122.43	46.01	4.80	31.67	−1.38	0.35(2.44)	0.12	−0.10	3.2
215954.45−002150.1	−29.20	5.10	$13.66^{+1.49}_{-1.35}$	6.51	27.64	45.36	7.94	31.89	−1.71	0.05(0.35)	0.75	0.07	2.8
113949.39+460012.9*	−27.38	2.26	$471.14^{+241.54b}_{-241.54}$	48.07	197.62	46.17	1.92	31.23	−1.15	0.52(3.21)	0.04	−0.30	3.5

Note. — Col. (1): Object name. The object marked with “*” comes from the extreme subsample. Col. (2): Absolute i -band magnitude. Col. (3): The column density of Galactic neutral hydrogen (Dickey & Lockman 1990). Col. (4): Soft-band (0.5–2 keV) count rate in units of 10^{-3} s^{-1} . Col. (5): Observed-frame 0.5–2 keV flux (corrected for Galactic absorption) in units of $10^{-14} \text{ erg cm}^{-2} \text{ s}^{-1}$. Col. (6): Flux density at rest-frame 2 keV in units of $10^{-32} \text{ erg cm}^{-2} \text{ s}^{-1} \text{ Hz}^{-1}$. Col. (7): Logarithm of the rest-frame 2–10 keV luminosity in units of erg s^{-1} , derived from Γ_{eff} and the observed-frame 0.5–2 keV flux. Col. (8): Flux density at rest-frame 2500 Å in units of $10^{-27} \text{ erg cm}^{-2} \text{ s}^{-1} \text{ Hz}^{-1}$. Col. (9): Logarithm of the rest-frame 2500 Å luminosity density in units of $\text{erg s}^{-1} \text{ Hz}^{-1}$. Col. (10): Observed α_{OX} . Col. (11): The difference between the observed α_{OX} and the expectation from the $\alpha_{\text{OX}}-L_{2500 \text{ \AA}}$ relation (Just et al. 2007). In the parentheses, the statistical significance of this difference is presented in units of the α_{OX} rms scatter from Table 5 of Steffen et al. (2006). Col. (12): The factor of X-ray weakness. Col. (13): Relative SDSS $g-i$ color. Col. (14): Radio-loudness parameter.

*For *RASS2RXS* data, the count rate is for 0.1–2.4 keV.

^bFor *XMMSL2* data, the count rate is for 0.2–2 keV.

Table 4. Stacked X-ray Properties of X-ray Weak Quasars in the Representative Sample

Sample	N_{weak}	Mean Redshift	Total Stacked Exposure (ks)	Soft-Band Counts	Hard-Band Counts	Γ_{eff}	α_{OX}	$\Delta\alpha_{\text{OX}}(\sigma)$	$s(\Delta\alpha_{\text{OX}})$
(1)	(2)	(3)	(4)	(5)	(6)	(7)	(8)	(9)	(10)
Extreme	7	1.823	22.9	< 3.9	< 2.5	...	< -2.33	< -0.64(4.17)	...
Bridge	7	1.945	30.0	$12.2^{+4.8}_{-3.6}$	$11.5^{+4.9}_{-3.6}$	$1.09^{+0.55}_{-0.45}$	-2.14	-0.45(2.93)	0.11
Representative	14	1.884	52.9	$13.2^{+4.9}_{-3.7}$	$11.2^{+4.9}_{-3.6}$	$1.19^{+0.56}_{-0.45}$	-2.22	-0.53(3.44)	0.10

Note. — Col. (1): Sample or subsample name. Col. (2): Number of X-ray weak WLQs in the sample (or subsample). Col. (3): Mean redshift of X-ray weak WLQs in the sample (or subsample). Col. (4): The total *Chandra* exposure time of X-ray weak WLQs in the sample (or subsample). Cols. (5) and (6): Aperture-corrected stacked net counts in the soft (0.5–2 keV) and hard (2–8 keV) bands. If the source is not detected, an upper limit at a 90% confidence level is listed. Col. (7): See the note of Col. (11) in Table 2. Cols. (8)–(9): See the note of Cols. (10)–(11) in Table 3. Col. (10): Estimated error of the stacked $\Delta\alpha_{\text{OX}}$ based on bootstrapping counts.

Table 5. UV Emission-Line Measurements of Quasars in the Bridge Subsample from the SDSS Spectra

Object Name (J2000)	MJD	C IV Blueshift (km s ⁻¹)	C IV FWHM (km s ⁻¹)	REW C IV	REW Si IV	REW $\lambda 1900 \text{ \AA}$	REW Fe II	REW Fe III	REW Mg II
(1)	(2)	(3)	(4)	(5)	(6)	(7)	(8)	(9)	(10)
Chandra Cycle 17 Objects									
080040.77 + 391700.4	55528	-2384 ± 114	7058 ± 565	13.5 ± 0.5	8.6 ± 0.6	15.8 ± 0.6	24.5 ± 1.2	5.5 ± 0.6	21.9 ± 1.1
095023.19 + 024651.7	51908	-3675 ± 834	5380 ± 421	8.0 ± 1.7	7.5 ± 2.1	17.1 ± 2.0	33.5 ± 3.6	5.0 ± 1.8	23.9 ± 4.1
101209.62 + 324421.4	53442	-2865 ± 419	8497 ± 627	12.5 ± 1.6	8.0 ± 1.8	18.3 ± 1.9	31.7 ± 6.0	5.2 ± 1.4	23.2 ± 3.6
101945.26 + 211911.0	56027	-155 ± 43	2352 ± 204	13.1 ± 0.6	5.1 ± 0.7	11.7 ± 0.8	10.0 ± 1.5	4.1 ± 0.8	17.5 ± 1.2
110409.96 + 434507.0	53053	-483 ± 279	5187 ± 415	10.8 ± 1.5	14.2 ± 2.2	13.5 ± 1.5	28.5 ± 2.7	4.7 ± 1.6	26.0 ± 2.9
122048.52 + 044047.6	52378	-3488 ± 444	10361 ± 793	12.1 ± 1.4	...	15.5 ± 1.4	28.5 ± 2.4	5.6 ± 1.7	28.7 ± 2.2
122311.28 + 124153.9	56308	-3547 ± 531	9531 ± 730	7.8 ± 0.9	5.8 ± 0.9	11.3 ± 1.2	29.1 ± 2.4	4.0 ± 1.1	20.3 ± 2.7
122855.90 + 341436.9	55571	-972 ± 107	2979 ± 239	7.0 ± 0.6	4.3 ± 0.6	8.0 ± 0.9	18.5 ± 1.8	1.7 ± 0.7	11.5 ± 1.8
124516.46 + 015641.1	52024	-3069 ± 245	7876 ± 622	13.3 ± 1.0	7.4 ± 1.0	18.4 ± 1.6	21.5 ± 3.1	3.0 ± 1.1	25.8 ± 3.4
140701.59 + 190417.9	56039	-5723 ± 397	10651 ± 798	8.4 ± 1.0	5.5 ± 0.9	18.7 ± 1.6	27.6 ± 2.9	2.6 ± 1.2	23.8 ± 2.5
150921.68 + 030452.7	55652	-1869 ± 112	6715 ± 517	15.5 ± 0.7	6.2 ± 0.8	18.2 ± 0.8	23.3 ± 1.5	4.8 ± 0.8	20.9 ± 1.2
155621.31 + 112433.2	54572	233 ± 87	2834 ± 227	9.3 ± 0.8	...	10.7 ± 0.8	19.6 ± 1.5	1.6 ± 0.8	20.2 ± 1.4
163810.07 + 115103.9	54585	-1153 ± 141	4485 ± 360	11.1 ± 0.9	7.9 ± 1.0	10.7 ± 1.2	13.8 ± 2.1	1.4 ± 0.9	18.7 ± 2.4
232519.33 + 011147.8	51818	-5208 ± 523	6564 ± 526	7.4 ± 1.9	...	12.8 ± 1.7	30.0 ± 3.1	5.8 ± 2.0	25.4 ± 3.1
Archival Data									
123326.03 + 451223.0	56367	-1091 ± 61	3877 ± 310	10.9 ± 0.6	5.8 ± 0.5	14.4 ± 0.8	21.8 ± 1.6	3.6 ± 0.7	19.8 ± 1.3
215954.45 - 002150.1	52173	-163 ± 65	2698 ± 216	7.4 ± 0.6	4.6 ± 0.6	8.9 ± 0.8	15.8 ± 1.4	1.5 ± 0.6	13.8 ± 1.3
113949.39 + 460012.9*	56398	-3408 ± 413	7808 ± 656	5.7 ± 0.7	5.0 ± 0.7	9.4 ± 1.2	24.9 ± 2.0	2.1 ± 1.0	13.5 ± 1.8

Note. — Col. (1): Object name. The object marked with “*” comes from the extreme subsample. Col. (2): Modified Julian date of the SDSS observation. Cols. (3)–(5): Blueshift, full width at half maximum (FWHM), and REW (in units of \AA) of C IV $\lambda 1549$. Cols. (6)–(10): REWs (in units of \AA) of the Si IV $\lambda 1397$, $\lambda 1900$ complex, Fe II (2250–2650 \AA), Fe III UV48 $\lambda 2080$, and Mg II $\lambda 2799$ emission features. The Si IV $\lambda 1397$ feature is a mixture of Si IV and O IV]. The $\lambda 1900$ complex mainly consists of C III] $\lambda 1909$, and it also includes [Ne III] $\lambda 1814$, Si II $\lambda 1816$, Al III $\lambda 1857$, and Si III] $\lambda 1892$. “...” indicates insufficient spectral coverage for accurate measurements.

Table 6. X-ray Weakness Properties of Quasar Subsamples

Sample Name	Sample Properties			P_{null} of Fisher's Exact Test			
	Median $\Delta\alpha_{\text{OX}}$	N_{weak}	F_{weak}	Extreme Subsample	Bridge Subsample	Gibson et al. (2008) Subsample 1	Gibson et al. (2008) Subsample 2
	(1)	(2)	(3)	(4)	(5)	(6)	(7)
Extreme Subsample	$-0.10^{+0.12}_{-*}$	7	$43.8\%^{+12.4\%}_{-11.0\%}$	1	1	5×10^{-4}	1×10^{-4}
Bridge Subsample	$-0.19^{+0.04}_{-*}$	7	$43.8\%^{+12.4\%}_{-11.0\%}$	1	1	5×10^{-4}	1×10^{-4}
Gibson et al. (2008) Subsample 1	$-0.02^{+0.01}_{-0.02}$	3	$5.1\%^{+4.5\%}_{-1.6\%}$	5×10^{-4}	5×10^{-4}	1	0.68
Gibson et al. (2008) Subsample 2	$0.05^{+0.02}_{-0.02}$	2	$3.3\%^{+4.1\%}_{-1.1\%}$	1×10^{-4}	1×10^{-4}	0.68	1

Note. — Col. (1): Median $\Delta\alpha_{\text{OX}}$ values of each subsample. The 1σ uncertainties of $\Delta\alpha_{\text{OX}}$ are estimated via bootstrap. *For the extreme subsample and the bridge subsample, the 1σ lower bound of median $\Delta\alpha_{\text{OX}}$ cannot be appropriately estimated as a result of having too many upper limits in the sample with unknown distributions. Col. (2): Number of X-ray weak quasars in each subsample. Col. (3): The fraction of X-ray weak quasars with uncertainties calculated following Cameron (2011). Cols. (4)–(7): Probabilities of the two corresponding subsamples having an equal fraction of X-ray weak quasars using Fisher's exact test.

Table 7. Results from Peto-Prentice Tests Comparing the Spectral Properties of X-ray Weak and X-ray Normal WLQs

Spectral Property	Representative Sample				Full sample			
	N_{weak}	N_{normal}	σ	P_{null}	N_{weak}	N_{normal}	σ	P_{null}
C IV REW	14	18	0.3	0.79	26	20	0.03	0.98
C IV blueshift	14	18	0.4	0.67	26	19	1.4	0.16
C IV FWHM	14	18	0.08	0.94	26	19	1.0	0.31
Si IV REW	9	13	0.3	0.74	24	19	0.06	0.95
$\lambda 1900 \text{ \AA}$ REW	14	18	0.6	0.57	32	26	0.2	0.86
Fe II REW	14	18	1.5	0.14	32	28	3.1	2×10^{-3}
Fe III REW	14	18	0.9	0.38	32	28	0.9	0.35
Mg II REW	14	16	0.5	0.65	27	25	0.7	0.47
$\Delta(g-i)$	14	18	2.4	0.01	33	26	3.9	1×10^{-4}

Note. — The Peto-Prentice test was performed for both the representative sample and the full sample. It reduces to Gehan's Wilcoxon test when there is no censoring. For each spectral property, we list the number of X-ray weak WLQs (N_{weak}) and the number of X-ray normal WLQs (N_{normal}) available for the test, the test statistic (σ), and the probability of the distributions of this spectral property among X-ray weak WLQs and X-ray normal WLQs being drawn from the same population.

This paper has been typeset from a $\text{\TeX}/\text{\LaTeX}$ file prepared by the author.